remote sensing

MDPI

Article

Multi-Source SAR-Based Surface Deformation Monitoring and Groundwater Relationship Analysis in the Yellow River Delta, China

Yilin Liu [1,2,3], Yi Zhang [4], Faqiang Zhao [1,3], Renwei Ding [1], Lihong Zhao [1], Yufen Niu [5], Feifei Qu [6] and Zilong Ling [1,*]

[1] College of Earth Science and Engineering, Shandong University of Science and Technology, Qingdao 266590, China; liu@sdust.edu.cn (Y.L.)
[2] Key Laboratory of Marine Geology and Environment, Institute of Oceanology, Chinese Academy of Sciences, Qingdao 266071, China
[3] Shandong Institute of Geophysical and Geochemical Exploration, Jinan 250013, China
[4] College of Ocean Science and Engineering, Shandong University of Science and Technology, Qingdao 266590, China
[5] School of Mining and Geomatic Engineering, Hebei University of Engineering, Handan 056038, China
[6] Department of Earth Sciences, Southern Methodist University, Dallas, TX 75025, USA; fqu@smu.edu
* Correspondence: lingzilong@sdust.edu.cn

Abstract: Land motions are significantly widespread in the Yellow River delta (YRD). There is, however, a lack of understanding of the delta-wide comprehensive deformation mode and its dynamic mechanism, especially triggered by groundwater extraction. This paper adopts an integrated analysis of multidisciplinary data of image geodesy, geophysics, geology and hydrogeology to provide insights into Earth surface displacement patterns and dynamics in the YRD. Delta-scale land motions were measured for the first time using L-band ALOS images processed using multi-temporal InSAR, illustrating multiple obvious surface sinking regions and a maximum annual subsidence velocity of up to 130 mm. Then, the InSAR-constrained distributed point source model with optimal kernel parameters, a smoothness factor of 10 and a model grid size of 300 m was established and confirmed to be rational, reliable and accurate for modeling analysis over the YRD. Remarkable horizontal surface displacements, moving towards and converging on a sinking center, were recovered by means of modeling and measured using InSAR, with a maximum rate of up to 60 mm per year, which can trigger significant disasters, such as ground fissures and building damage. In addition, the annual total water storage variation at the delta scale, the most meaningful outcome, can be calculated and reaches a total of approximately 12,010 $\times$ 10^3 m^3 in Guangrao city, efficiently filling the gap of GRACE and in situ investigations for delta-wide aquifer monitoring. Finally, a comparative analysis of time series InSAR measurements, modeling outcomes, and fault and groundwater data was conducted, and the strong agreement demonstrates that faults control aquifer distribution and hence the spatial distribution of groundwater-withdrawal-related regional land subsidence. Moreover, the obvious asymmetric displacements, demonstrating a northeasterly displacement trend, further reveal that faults control aquifer distribution and Earth surface deformation. These findings are useful for understanding the land motion patterns and dynamics, helping to sustainably manage groundwater and control disasters in the YRD and elsewhere worldwide.

Keywords: land motion; multi-temporal InSAR; distributed point source model; horizontal displacement; groundwater; fault; the Yellow River delta

Citation: Liu, Y.; Zhang, Y.; Zhao, F.; Ding, R.; Zhao, L.; Niu, Y.; Qu, F.; Ling, Z. Multi-Source SAR-Based Surface Deformation Monitoring and Groundwater Relationship Analysis in the Yellow River Delta, China. *Remote Sens.* **2023**, *15*, 3290. https://doi.org/10.3390/rs15133290

Academic Editor: Cristiano Tolomei

Received: 29 April 2023
Revised: 13 June 2023
Accepted: 25 June 2023
Published: 27 June 2023

1. Introduction

Today, more than half a billion people live on or near river deltas [1]. Increasing population numbers, expanding agricultural and industrial regions and socioeconomic development cause an increasing demand for water in deltas. This is particularly evident

for densely populated mega-deltas, where groundwater is often exploited as an additional freshwater source [2,3]. However, with long-term excessive groundwater withdrawal, groundwater depletion can occur. The resulting lowering of the groundwater table can trigger delta sinking [4,5]. Populous and low-lying delta plains are particularly highly vulnerable to a variety of hazards associated with groundwater-extraction-induced submergence [6–9]. Therefore, detailed investigations of delta surface deformation and insights into its dynamics are critical to the management of groundwater sustainable development, hazard prevention and mitigation, and delta environmental sustainability.

The space-borne Interferometric Synthetic Aperture Radar (InSAR) technique has rapidly developed and now allows for accurate mapping of surface displacement with high spatiotemporal resolution [10–16]. In addition, compared to traditional methods, InSAR has broad coverage, high sensitivity to ground motion, and high spatiotemporal resolution regardless of weather conditions [17,18]. This is achieved using multiple images and advanced analysis methods, making InSAR a reliable and effective approach for studying surface displacement in deltaic environments [12,14,19–21]. Nevertheless, high-quality deltaic InSAR measurement is still challenging because river deltas are always densely vegetated, which can result in serious phase decorrelation [22]. Therefore, the implementation of advanced algorithms, such as Persistent Scatter (PS) [23] and Small BAseline Subset (SBAS) [24], is fundamental for the investigation of delta sinking processes. The Stanford Method for Persistent Scatterers (StamPS) SBAS operation adopted here has the advantages of operating on single-look interferograms and requiring no prior knowledge of surface deformation [25–27] and can retrieve as much reliable ground information as possible over the vegetated delta plain. Moreover, image data with a relatively longer wavelength (λ), e.g., the L-band SAR data (λ = 23.6 cm), have a comparatively high spatio-temporal coherence over longer time periods, and many images are available for the delta plain. Correspondingly, the utilization of L-band SAR images can be effective in promoting the detectability and measurement accuracy of delta surface deformation.

Numerous major river deltas worldwide have witnessed severe regional land subsidence induced by groundwater pumping [7,28,29]. However, comprehensive investigations of the role of groundwater extraction in triggering surface sinking in delta plains are scarce. In addition, despite being a significant environmental indicator and leading to obvious delta land sinking, groundwater deficit is often poorly recognized at the delta scale. The hydraulic head and storage changes generally depend on temporal responses to groundwater stresses, measured as water table changes in wells. Yet, the ground-based monitoring wells are usually shallow and sparsely distributed, and individual well tends to indicate the local status of the penetrated critical aquifers [30]. Moreover, the exact locations of most pumping wells are not known, and water withdrawal is often unrestricted and unmonitored, in particular in agricultural regions where landowners developed private wells. Happily, the satellite-based Gravity Recovery and Climate Experiment (GRACE) [31], sensitive to total water storage (TWS) variations, can overcome the limitations of ground-based methods and has greatly contributed to estimating changes in groundwater storage (GS) over large regions [32–34]. Nevertheless, limited by insufficient spatial resolution, GRACE struggles to measure water mass variations over small watersheds. It is thus unable to estimate TWS changes at local or regional (100–10,000 km^2) scales, e.g., a delta plain, where groundwater issues are focused on and most groundwater management policies are implemented [31,34]. A wide gap, therefore, exists in delta-scale GS variation monitoring between the direct observations of ground-based point wells and space-based GRACE.

It is from this perspective that image geodesy can provide suitable Earth surface displacement observations to characterize deltaic GS changes at the intermediate scale between borehole log data and GRACE. The over-abstraction of groundwater resources can result in a severe drawdown of hydraulic heads (i.e., groundwater levels) [8]. This process is known to reduce pore pressure and effective stress within the aquifer and hence trigger consolidation and compaction of the fine-grain sedimentary layer, which is expressed as subsidence of the delta land surface [35,36]. Thus, the observed land subsidence, in turn, can

be used to estimate relative aquifer changes. Because this is an indirect form of monitoring, however, further additional analysis is needed to estimate the pressure or volume changes within the hydrogeological unit. Specifically, inverse problems must be solved to tie surface deformation to GS variations. Numerical modeling, combined with deformation results and geotechnical parameters, is critical for the inversion of GS variations. InSAR-constrained modeling, therefore, can link GS variations to surface deformation and simultaneously invert GS variations in delta plains with improved spatiotemporal resolution compared to field investigations and GRACE.

Additionally, in terms of surface displacement related to groundwater deficit, accompanying vertical land motion, significant surface horizontal displacement also occurs [37–39]. Nevertheless, almost all InSAR measurements to date have been performed under the assumption that delta surface deformation is purely vertical (i.e., land subsidence) [14,40–42]. This assumption can greatly simplify processes of InSAR measurement and numerical modeling related to delta aquifer system changes. However, a river delta is a depositional sedimentary body where fine-grained sediments with high porosity and compressibility (e.g., soft clay) are always extensively developed. Neglecting the lateral shear stress of the horizontal displacement, which often has significant damaging effects, could be even more hazardous to deltaic buildings and infrastructures. Accordingly, measurements and analysis of deltaic horizontal displacement are also significant to disaster control and environmental sustainability over delta plains.

Here, we first mapped the detailed spatiotemporal subsidence patterns over YRD using multi-band images processed by the multitemporal InSAR technique. Then, Earth surface displacements were linked to groundwater mining. Meanwhile, InSAR-constrained numerical modeling was developed to monitor GS variations. In addition, delta three-dimensional (3D) displacements induced by groundwater pumping were retrieved and analyzed. Furthermore, an integrated analysis of multidisciplinary data of InSAR measurements, modeling outcomes, groundwater and faults was conducted to establish the dynamic mechanisms of surface displacement and the role of faults and groundwater deficit in the action of land subsidence and GS variations. The rest of this paper is organized as follows: Section 2 describes the study area and materials and methods; Section 3 analyzes the delta surface displacement results, including the obvious 3D deformation and modeling results; Section 4 discusses the optimal kernel model parameters, surface sinking mechanism and its relationship with GS variations and fault; and Section 5 provides the conclusion.

2. Materials and Methods

2.1. Study Area

The YRD is 1 of the major largest delta systems on Earth. Geographically located in the northern Shandong peninsula, China, bordering the southwest of the Bohai Sea, the delta plain covers a surface area of more than 5500 km^2 (Figure 1). It was formed in 1855 when the Yellow River altered its course from the south to the north and simultaneously flowed into the Bohai Sea instead of the Yellow Sea. The river is best known for having the highest sediment concentration among the world's longest rivers [43] and for frequent course shifting in the lower reaches [44], directly leading to the formation of the eastward fan-shaped delta plain [45,46].

Geologically, the YRD is located in the Jiyang sub-basin, southeast of the Bohai Bay basin [47]. The northeast-southwest trending sub-basin is controlled by a series of normal faults in an echelon pattern and thereby is divided into 5 secondary tectonic units, among which 2 present sags and 3 present uplifts (Figure 1) [48]. Hydrogeologically, affected by geomorphology, sediment and the structural environment, and seawater intrusion, the groundwater in YRD is mainly loose rock pore water occurring in the quaternary alluvial and marine sediment layer [49]. A hydrogeological cross-section from Guangrao Country to Dongying District, with the stratum divided into 8 geological formations, including 3 aquifers and 4 compressible clay layers, is demonstrated in Figure 1b and Appendix A

Table A1. Generally, 3 typical hydrogeological units can be distinguished: I, the Piedmont alluvial fan, with pure freshwater; II, the marine-continental depositional and alluvial-proluvial plain, with brackish water; and III, the YRD alluvial plain, with pure salt water (Figure 1a) [50].

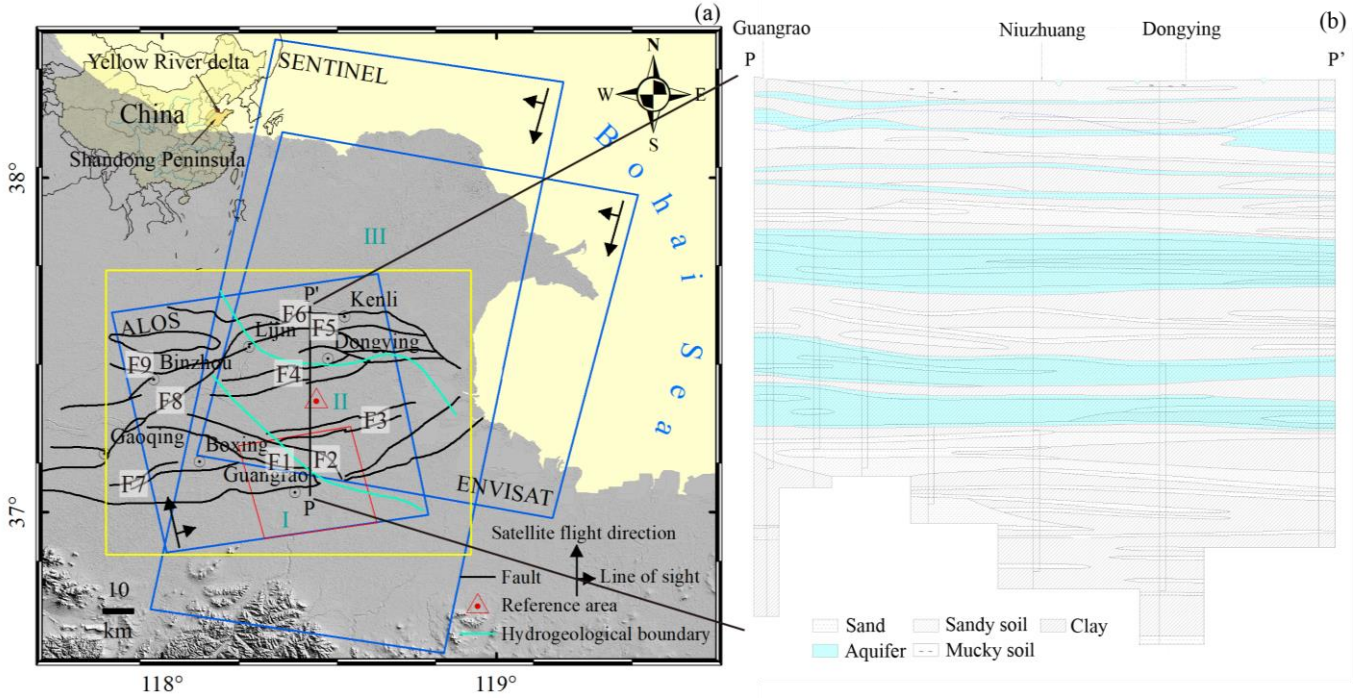

Figure 1. (**a**) An overview map of the study area. InSAR study areas are illustrated by blue quadrangles for ascending ALOS and descending ENVISAT and SENTINEL-1. The red quadrangle and yellow rectangle indicate the modeling area and the focal region in this study, respectively. F1–F9 are the Shicun Fault, Tonggu Fault, Chen'guanzhuang Fault, Central Fault Zone, Shengyong Fault, Chennan Fault, Boxing Fault, Gaoqing—Ping'nan Fault, and Binnan Fault, respectively. I, II and III denote the hydrogeological units. The base map is a shaded relief map. The top-left inset is the geographic location of the YRD. (**b**) Typical hydrogeological formations profile along the cross-section line P–P′.

The YRD has a typical warm-temperate and semi-humid continental monsoon climate, with an annual average rainfall of 530–630 mm and evaporation of 750–2400 mm [51]. The low precipitation and high evaporation in this region have accelerated the shortage of freshwater resources. This issue can be primarily addressed by means of underground freshwater exploitation. Numerous deep wells have been built and are still working. The extractions, at a mean annual volume of 90 million cubic meters, already far exceed recharge, while with rapid socioeconomic development, freshwater demand is increasing gradually, meaning that groundwater depletion is on the rise. The 2 small shallow groundwater funnels in the 1980s have expanded to 4 large deep ones in the present day.

2.2. SAR Data

Three types of images covering the YRD, ENVIronmental SATellite (ENVISAT) Advanced Synthetic Aperture Radar (ASAR), Advanced Land Observing Satellite (ALOS) Phased Array type L-band SAR (PALSAR) and Sentinel-1, were collected. The descending ENVISAT and Sentinel-1, working on C-band 56 mm wavelength, flies from north to south and faces the west, while the ascending ALOS, operating at L-band 236 mm wavelength, travels from south to north and looks to the east (Figure 1). A total of 195 images, including 29 from ENVISAT and 22 from ALOS spanning from 2007 to 2011 and 144 from Sentinel-1 during the period of 2016–2021, were utilized.

2.3. SBAS InSAR

The standard SBAS method usually unwraps the multi-looked and filtered interferograms individually. Meanwhile, the SBAS process in StamPS operates on single-look interferograms to identify the distributed scatterers with relatively stable phase characteristics in both time and space, which are defined as slow-varying filtered phase (SVFP) pixels [26,27]. This change can enable the SBAS to operate on the highest spatial resolution and identify the isolated SVFP pixels among completely decorrelated pixels and can also allow the effective measurement of deformation over the delta plain using the SBAS method.

To maximize the coherence and detectability, StamPS SBAS forms interferograms based on minimum spatiotemporal baselines and the Doppler frequency of SAR image pairs. The interferograms are then filtered in range and azimuth direction to reduce the geometric decorrelation effect and non-overlapping Doppler spectrum, respectively. The StamPS SBAS first identifies an initial set of persistent scatterer candidates (PSCs) using the amplitude dispersion index D_A:

$$D_A \equiv \sigma_A / \mu_A \tag{1}$$

where σ_A and μ_A are the standard deviation of the amplitude difference and the mean amplitude, respectively. Generally, a threshold value of the index (D_A) is used to select the PSCs. The final coherent points are then selected from the PSCs, using a measure of the decorrelation noise, γ_x, of the PSCs [26]:

$$\gamma_x = \frac{1}{N}\left|\sum_{i=1}^{N} exp\left\{\sqrt{-1}(\Psi_{x,i} - \widetilde{\Psi}_{x,i} - \Delta\widetilde{\Psi}^{u}_{\theta,x,i})\right\}\right| \tag{2}$$

where N is the number of interferograms, $\Psi_{x,i}$ is the wrapped phase from the x-th pixel in the i-th interferogram, $\widetilde{\Psi}_{x,i}$ denotes the wrapped estimate of the spatially correlated phase, including contributions of the surface deformation, the orbital error, the atmospheric delay, and the spatially correlated elevation error, and $\widetilde{\Psi}^{u}_{\theta,x,i}$ represents the estimate of the spatially uncorrelated phase due to both the spatially uncorrelated look angle and elevation error. The change in γ_x is calculated in each iteration and halts the computation when it ceases to decrease and tends to converge. A threshold value of γ_x is adopted for the final selection of SVFP pixels. The wrapped phases of the SVFP pixels in the time-series (TS) interferograms are unwrapped using a 3D phase unwrapping method [52]. Then, the unwrapped TS interferograms are filtered by a spatial low-pass filter and a temporal high-pass filter to reduce the remaining errors. Finally, the TS deformation at each SVFP location is retrieved using a least-squares inversion.

Here, the differential interferograms of ENVISAT and ALOS were processed using the Doris software, while those of Sentinel-1 were processed using the ISCE package. A total of 712 interferograms were constructed, including 136 from ENVISAT descending orbits, 78 from ALOS ascending orbits and 498 from Sentinel-1 descending orbits (Figure 2). To ensure temporal continuity in time-series analysis, some interferograms with spatial/temporal baselines exceeding the thresholds are also included (Figure 2). The flat-Earth and topography phases of each filtered interferogram were removed using a 1 arc-second Shuttle Radar Topography Mission (SRTM) Digital Elevation Model (DEM). A threshold value of $D_A = 0.6$ and $\gamma_x = 0.005$ was adopted for initial PSCs and final SVFP pixel selection, respectively. The 3 datasets were each processed using the above StamPS SBAS approach.

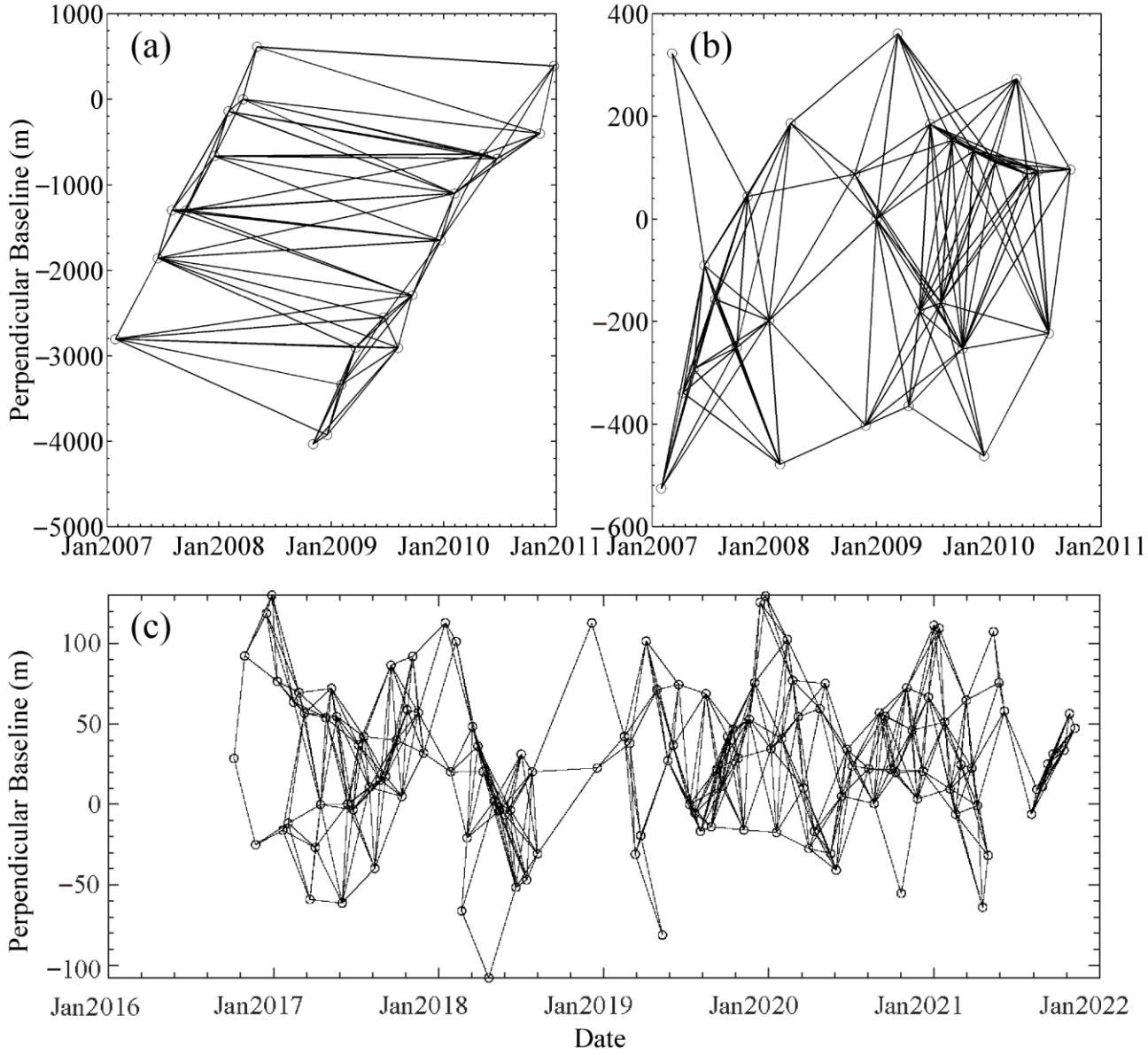

Figure 2. Spatial and temporal baseline configuration of SBAS interferograms of three datasets: (**a**) ALOS, (**b**) Envisat, and (**c**) Sentinel. Interferograms with perpendicular baselines less than 1200 m and temporal baselines less than 720 days for L-band ALOS data, perpendicular and temporal baseline thresholds of 500 m and 720 days for C-band Envisat data, and 75 m and 72 days for C-band Sentinel data.

2.4. Velocity Decomposition

The displacement velocity (v^{los}) of each SVDF derived from the SBAS approach is in the line-of-sight (LOS) direction and can be expressed as:

$$v^{los} = -uv, \tag{3}$$

where $v = (v^e, v^n, v^v)^T$ is the 3D displacement velocity (east, north, and up) in the local reference frame, and $u = (-sin\theta cos\alpha, sin\theta sin\alpha, cos\theta)$ is the unit of the LOS displacement vector in the same reference frame, where α and θ are the satellite heading angel and the radar incidence angle, respectively. Using the LOS results V^{los} from different geometries

(azimuth and incidence angels), the 3D displacement field ($\hat{v}$) can be recovered based on least-square inversion:

$$\hat{v} = -\left(U^T U\right)^{-1} U^T V^{los}, \tag{4}$$

where $V^{los} = \left(v_1^{los}, v_2^{los}, \cdots, v_n^{los}\right)^T$, $U = (u_1, u_2, \cdots, u_n)^T$, and $()^{-1}$ and $()^T$ represent the matrix inversion and transposition, respectively. For more details, see Fuhrmann and Garthwaite [53].

2.5. Distributed Point-Source Model

When groundwater is pumped from aquifers, the effective stress and pore pressure in the aquifer reduce, causing reservoir shrinkage, which can translate into detectable surface displacement. To link the measured deformation to aquifer parameters, geophysical modeling is essential. The point deformation source, often referred to as the nucleus-of-strain or Mogi source [54], can be integrated to estimate the impact of aquifer volumetric reduction on surface displacement. During the model establishment process, we lumped together the thickness of the aquifer or the size of the point source, the pressure change, the shear modulus, and Poisson's ratio of the half-space at the point source location and treated them as a whole for calculation.

Based on the principle of effective stress [55], the surface displacement (d) produced by the volumetric strain (ΔV) equivalent to pressure change of a point source embedded in a uniform, isotropic elastic half-space is given by [56,57]:

$$d = (d^e, d^n, d^v)^T = \frac{(1-v)\Delta V}{\pi} \frac{1}{R^3} (x, y, z)^T \tag{5}$$

where $d = (d^e, d^n, d^v)$ is the 3D displacement (east, north, and up) of a surface point $(x, y, 0)$ in a local reference frame, v is the Poisson's ratio, the point pressure source is centered at $(0, 0, -z)$, and $R = \left(x^2 + y^2 + z^2\right)^{1/2}$ is the radial distance from the nucleus-of-strain center to the surface point.

In practice, the nature of the aquifer under study is complicated. The distributed point pressure source method is typically the most common strategy for modeling. The surface displacement field, $D = (d_1, \cdots, d_N)^T$, of N measurement points can be produced by the superposition of a nucleus-of-strain array, $V = (\Delta V_1, \cdots, \Delta V_M)^T$, of $M (M < N)$ point sources distributed in the aquifer [58–60]:

$$GV = D, \tag{6}$$

where the coefficient matrix $G = \begin{bmatrix} g_{1,1} & \cdots & g_{1,M} \\ \vdots & \ddots & \vdots \\ g_{N,1} & \cdots & g_{N,M} \end{bmatrix}$ is the discrete Green's function related to each nucleus-of-strain, $g_{i,j} = (g^e_{i,j}, g^n_{i,j}, g^v_{i,j})^T = \frac{(1-v)}{\pi} \frac{1}{R^3_{i,j}} (x_i, y_i, z_j)^T$, $d_i = (d^e_i, d^n_i, d^v_i)^T$, $i = 1, \cdots, N, j = 1, \cdots, M$.

Equation (6) can be resolved using the least-square method. However, it is usually an ill-conditional problem, and regularization is required. In addition, global bias (B) may exist in the InSAR measurements of the surface displacement field (D^{los}), owing to the uniform signals or uncertainties in the reference frame. Meanwhile, for contrast purposes, the LOS direction displacements are modeled using the coefficient matrix

$G^{los} = \begin{bmatrix} g_{1,1}^{los} & \cdots & g_{1,M}^{los} \\ \vdots & \ddots & \vdots \\ g_{N,1}^{los} & \cdots & g_{N,M}^{los} \end{bmatrix}$, where $g_{i,j}^{los} = {g_{i,j}}^T u$. Thus, the system of Equation (6) with global bias (B) and smoothness (αL) constraint can be represented as:

$$\begin{bmatrix} G^{los} & 1 \\ \alpha L & 0 \end{bmatrix} \begin{bmatrix} V \\ B \end{bmatrix} = \begin{bmatrix} D^{los} \\ 0 \end{bmatrix}, \tag{7}$$

where α is the smoothing factor, L is the smooth Laplacian operator, and $D^{los} = (d_1^{los}, \cdots, d_N^{los})^T$. The solution of this regularization method (Equation (7), least square with smoothness and bias constraint, can be expressed as:

$$\hat{V} = (G^{los})^{-g}(D^{los} - B) \tag{8}$$

where $(G^{los})^{-g} = ((G^{los})^T G^{los} + \alpha L^T L)^{-1} (G^{los})^T$.

3. Results

3.1. InSAR Results and Analysis

The southern part of YRD was selected as the focal region in this study (see Figure 1 for the location), where (i) pure freshwater and underground freshwater are overexploited in the Piedmont alluvial fan, and (ii) sufficient geological and hydrological data ensure further analysis, compared with the northern region. Three displacement velocity field maps of the focal region over YRD (Figure 3) are achieved using ALOS, ENVISAT and Sentinel-1 images processed via the SBAS InSAR method in Section 2.3. The phase value of the red solid triangle area (see the location in Figure 3), where the Earth's surface is relatively stable and assumed to display no deformation, is selected as a reference phase for TS analysis. The blank space is the area with no data, owing to incoherence.

ALOS images, having a longer wavelength, can detect more surface displacement information. Displacement field maps of 2007 to 2011 derived from ALOS and ENVISAT measurements have a similar deformation pattern, and displacement velocities are consistent with leveling data along leveling lines (see details in Appendix B), suggesting that the deformation results obtained are reliable and accurate. Several subsidence centers can be identified, and the maximum subsidence rate ranges from -30 mm/year to up to -130 mm/year. The spatial distribution of subsidence differs throughout the region. Region-wide sinking exists in Dongying City and Binzhou City in the northern part of the study area, while in the southern part, multiple obvious subsidence funnels have formed in Guangrao City and Boxing City. In addition, the subsidence pattern of bowl-shaped topographical depression is more marked in Guangrao City.

Spatially, similar to the subsidence pattern of ALOS and ENVISAT during the period of 2007 to 2011, the displacement velocity field map during the period of 2016 to 2021 from Sentinel-1 also illustrates that several remarkable subsidence regions exist in the focal study area, with maximum subsidence velocity ranging from -50 to up to -120 mm/year. In terms of time, meanwhile, the location and rate of significant local subsidence undergo certain changes. The Earth's surface in Dongying City and Binzhou City was relatively stable, with no subsidence during the observation period of 2016 to 2011, while there existed maximum subsidence with a rate of approximately -30 mm/year during the period of 2007 to 2011. In addition, two coastal sinking regions occurred during the period of 2016–2021 when compared with the period of 2007–2010, trigged by aquaculture activities [9]. Specifically, no significant changes in subsidence rate over time can be measured in Guangrao City and Boxing City during the two observation periods, where the subsidence triggered by natural sediment compaction was verified as being negligible [42,61,62]. Moreover, the effects of hydrocarbon extraction can also be excluded because no oil field is located in or near the subsidence regions. However, underground freshwater is pumped for domestic, agricultural, industrial, and

environmental purposes in this area, and groundwater overexploitation is widespread in the focal region. Therefore, remarkable long-term subsidence could be caused by unregulated groundwater extraction. Given this, we modeled and focused our further analysis on the land subsidence triggered by groundwater extraction in the southern part of YRD.

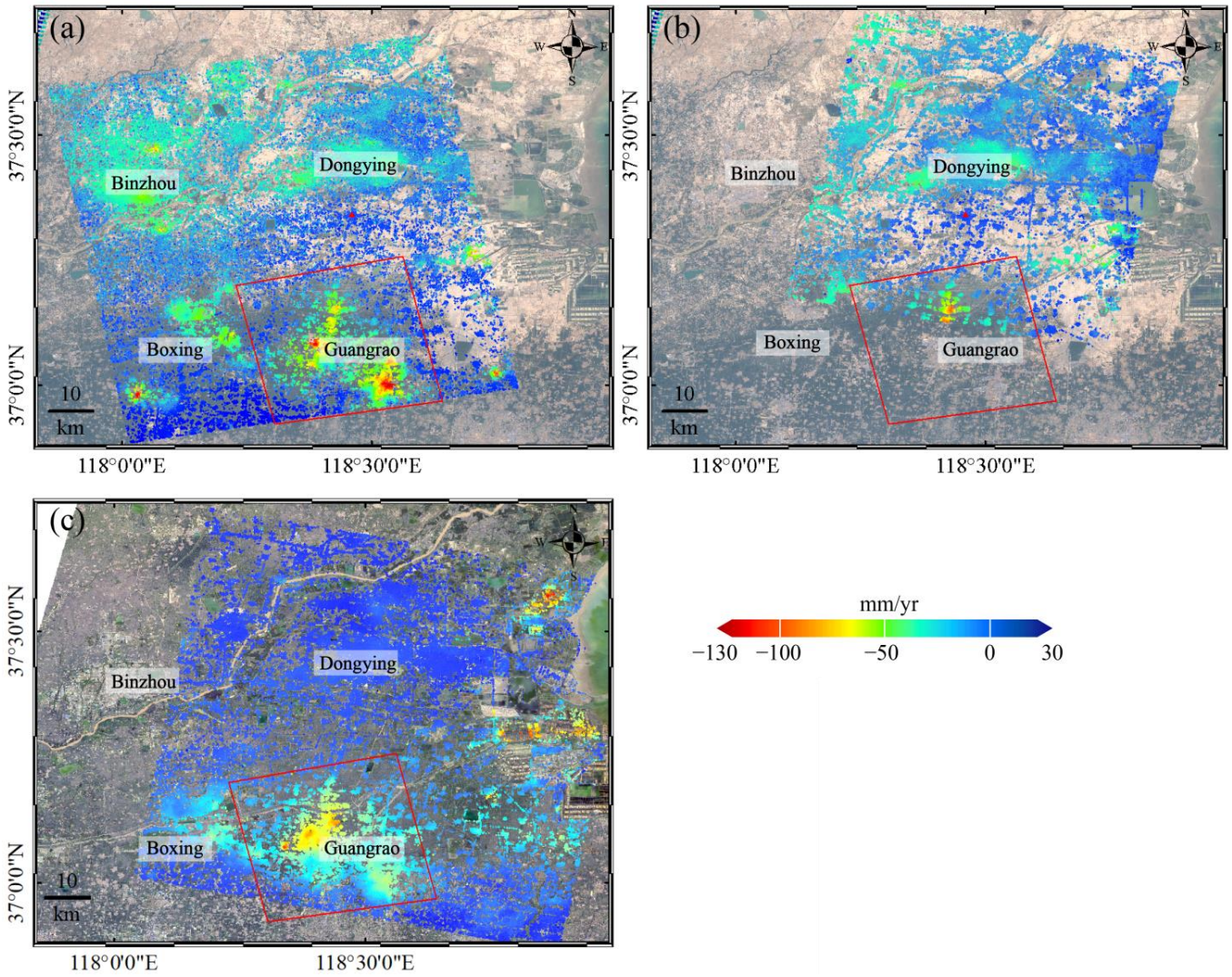

Figure 3. Annual mean velocity field map of InSAR during the period of 2007–2011 from ALOS (**a**), ENVISAT (**b**) and spanning from 2016 to 2021 from Sentinel-1 (**c**). The solid red triangle and open quadrangle denote the reference area and the modeling region, respectively. To ensure temporal coherence, the base maps in (**a**,**b**) are the natural-color images from NASA's Landsat satellite acquired on 3 May 2009, while that of (**c**) was obtained on 20 July 2020.

Although spatially, the displacement pattern of ALOS and ENVISAT measurements during the period of 2007 to 2011 is consistent, there are some differences in the deformation velocity, especially over the subsidence funnel area. The displacement velocity differences of two measurements exemplified by the modeling region (red open quadrangle area in Figure 3) were calculated, ranging from approximately −22 mm/year to 13 mm/year (Figure 4a). Correspondingly, the linear regression line of the cross-validation data of two measurements in the modeling region, with a slope value of 0.83, is slightly off the 1:1 line, which is more obvious for the larger displacement velocity points (Figure 4b). In addition, the expectation of the velocity differences, with a value of −5.2 mm/year, is non-zero (Figure 4c). These three deviations all demonstrate that horizontal displacement should be considered and further calculated in the study area.

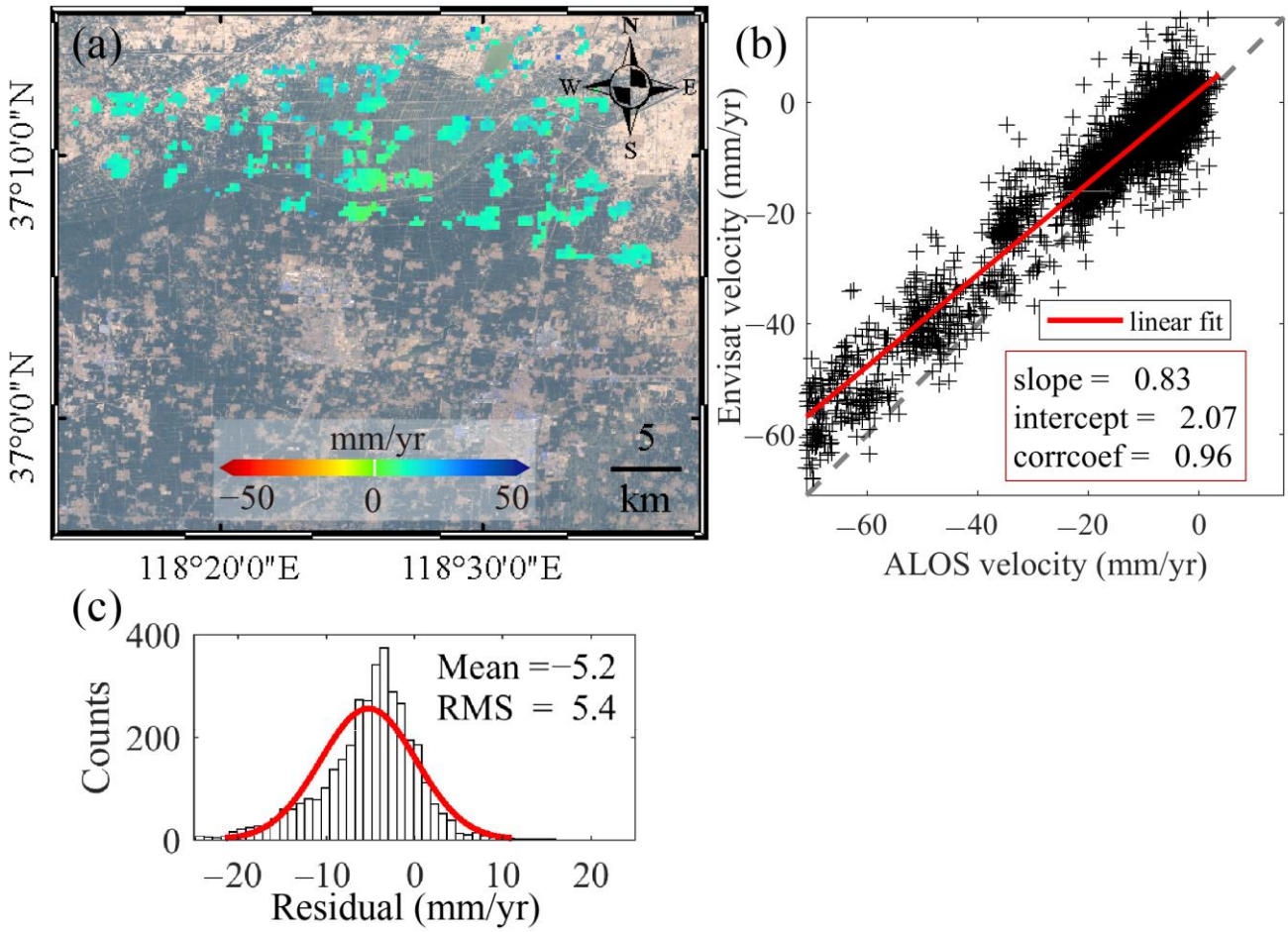

Figure 4. Comparison of ALOS and ENVISAT measurements over the modeling area (the red open quadrangle region in Figure 3). (**a**) Deformation velocity differences of measurements from ALOS and ENVISAT for the common pixels. The map was produced by the subtraction of the velocity value from ALOS from that from ENVISAT. (**b**) Cross-validation of the two measurements in the modeling region. The scatter plot denotes the common points. The solid red line and gray dashed line represent the linear regression and 1:1 line, respectively. (**c**) The corresponding histogram of (**a**) and its fitted normal curve.

Therefore, the horizontal displacement velocity map was calculated using ALOS and ENVISAT measurements based on the method described in Section 2.4. Because both the ascending and descending SAR satellites are in a near-polar orbit, the LOS displacement is not sensitive to displacement in the north-south direction. Thus, the north-south velocity cannot be measured using the ascending and descending SAR data alone. By eliminating this component, $u = (-sin\theta cos\alpha, cos\theta)$ in Equation (3), the 2D displacement $v = (v^e, v^v)^T$ (Figure 5a,b) can be recovered on the basis of Equation (4). Meanwhile, based on uncertainty propagation theory [63] and Equation (4), the standard deviations of the easterly (σ_e) and vertical velocity (σ_v; Figure 5c,d) can be calculated using the following equation:

$$\begin{pmatrix} \sigma_v^2 & cov_{ve} \\ cov_{ev} & \sigma_e^2 \end{pmatrix} = C \cdot \begin{pmatrix} \sigma_{ALOS}^2 & cov_{ALOS,Envisat} \\ cov_{Envisat,ALOS} & \sigma_{Envisat}^2 \end{pmatrix} \cdot C^T \quad (9)$$

where cov_{ve} and cov_{ev} are the covariances between the easterly and vertical velocities, $C = -(U^T U)^{-1} U^T$, $cov_{ALOS,Envisat}$ and $cov_{Envisat,ALOS}$ are the covariances between the velocities of ALOS and ENVISAT, and σ_{ALOS}^2 and $\sigma_{Envisat}^2$ are the variances of the velocities of ALOS and ENVISAT, respectively.

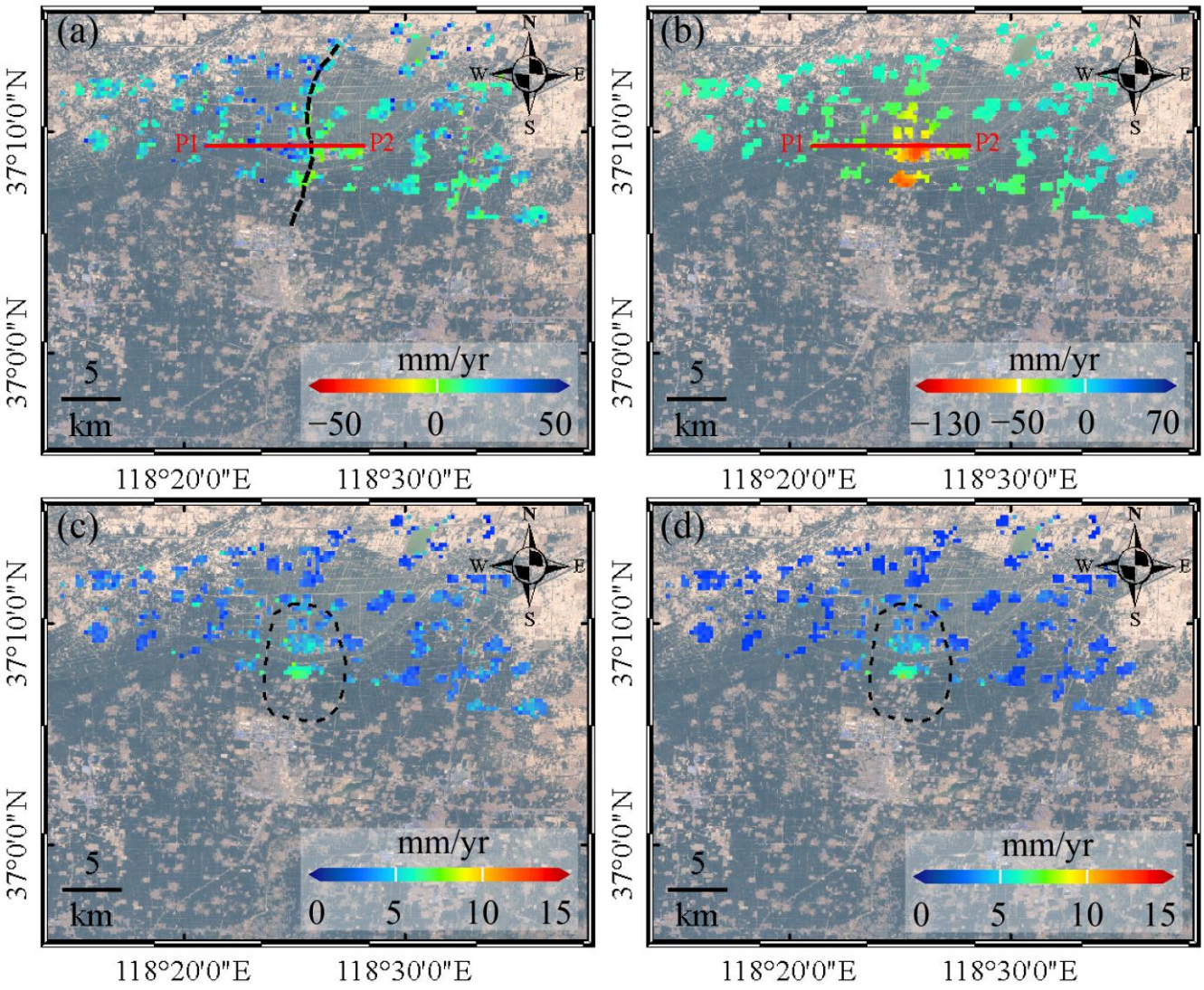

Figure 5. Velocity decomposition. (**a**,**b**) depict the east-west and vertical displacement, respectively. Positive values (i.e., red to green color points) and negative values (i.e., green to blue color points) in (**a**) represent eastward and westward displacement, respectively. (**c**,**d**) depict the corresponding standard deviation of (**a**) and (**b**), respectively. The red profile line (P1–P2) and black dashed curve are selected for 3D displacement comparison analysis. The figure extent is the same as in Figure 4.

Remarkable horizontal displacements can be detected, which are particularly striking around the black dashed line (Figure 5a). Significant eastward displacements exist in the region on the left, while westward displacements occur over the area on the right. The bilateral Earth surfaces, moving towards each other in opposite directions, converge on the center of a bowl-shaped subsidence funnel (Figure 5b), which conforms to the surface deformation triggered by subsurface pressure or volume reduction. The uncertainty in the central region of the subsidence funnel (black dashed polygon area in Figure 5c,d) is relatively high, with the mean standard deviation being larger than 5 mm/year, which can be accounted for by ignoring the north-south displacement and the larger vertical subsidence velocity over the depression center. Nonetheless, both the east-west and vertical deviations as a whole are small (Figure 5c,d), with a mean standard deviation of less than 3 mm/year, indicating that the calculated 2D displacement velocity fields are reliable.

3.2. Modelling Results and Analysis

Underground pressure or volume change can induce detectable surface deformation. In turn, the displacement velocity field can provide valuable constraints and help to model the reservoir change. A displacement velocity field derived from ALOS was used as the constraint for modeling because (i) more Earth surface information can be detected by the ALOS images in the focal region compared with ENVISAT images, which contributes to obtaining better modeling results, and (ii) the ALOS observation period (2007–2011) is consistent with the year of hydrological data (2009), which helps us to carry out the comparison and validation analysis.

Numerical modeling, a corresponding relationship between equivalent volume change of deep confined aquifer and InSAR-based subsidence, was performed using the inversion method described in Section 2.5 (Figure 6). To ensure consistency, the 3D surface displacement model was transformed into LOS displacement using LOS unit vectors during the modeling process. The InSAR LOS results of 68,103 selected pixels were used as constraints for modeling. Additionally, Poisson's ratio was set to 0.25 in this study, and the model depth (z in Equation (5)) was fixed at approximately 350 m, as deep groundwater was abstracted from a depth of 250–450 m in Dongying City. The reservoir was divided into 15,070 independent equal squares (Equation (6)) with an optimal width of 300 m, determined in Section 4.1.2. The least-squares method was adopted to calculate the source volume change. To achieve a reliable inversion and accurately represent the source, a Laplacian regularization technique (Equations (7) and (8)) with an optimal smoothing factor of 10, determined in Section 4.1.1, was applied to constrain and smooth the source strength.

The calculation results show that the modeling outcomes (Figure 6b) are in accordance with InSAR observations (Figure 6a), whether on deformation pattern or velocity. Figure 6c represents the differences between InSAR measurements and modeling results, and Figure 6d shows the corresponding statistical histogram. The differences are less than 10 mm/year, and the mean value and standard deviation are approximately 0 mm/year and 1.8 mm/year, respectively. These results further indicate the reliability and accuracy of the modeling outcomes.

The recovered 3D displacement velocity field maps (Figure 6e–g) illustrate that substantial north-south and east-west direction displacements occur in the study area, although the surface deformation is dominated by vertical displacement. The maximum annual north-south and east-west displacements reach up to 60 mm and 50 mm, respectively. The vertical displacement field shares similar deformation features with InSAR observations, with a maximum sinking rate of up to 130 mm/year in the depression center. The dividing line between northerly and easterly displacement coincides with an east-west-direction curve crossing the sinking center (Figure 6e). That is, the Earth's surface of the northern part moves southwards, while the southern part's Earth's surface moves northwards, converging on the dividing line. For east-west-direction displacement, the case is similar; what differs is that the dividing lines are south-north-direction curves (Figure 6f). The calculated horizontal displacement velocity field map (Figure 6i) shows pronounced horizontal Earth-surface movement around the subsidence funnel, with a maximum annual rate of up to 66 mm. The horizontal centripetal displacement demonstrates that the Earth's surface moves towards the central area in a horizontal orientation.

The outcomes of modeled underground source volume change (Figure 6h) show that remarkable groundwater extraction occurred in Guangrao city, with an annual exploitation quantity of $-11{,}063$ to 2469 m^3 in each unit (square grid of side length 300 m), equivalent to a TWS variation of $-12{,}010 \times 10^3$ m^3/year over the modeling region. However, in situ data of groundwater withdrawals are either unpublished or cannot be accessed, meaning that our modeling outcomes cannot be validated with on-site measurements. Fortunately, the annual deep groundwater pumping quantity is known at approximately $15{,}000 \times 10^3$ m^3/year in Guangrao City [64], which is consistent with our modeling results, and both are in the same order of magnitude. The underestimation of the model accounts for the fact that (i) the modeling area is part of the administrative region of Guangrao City, where several other

mining areas are present, and (ii) the grid-pattern model can reduce the total modeled reservoir volume change.

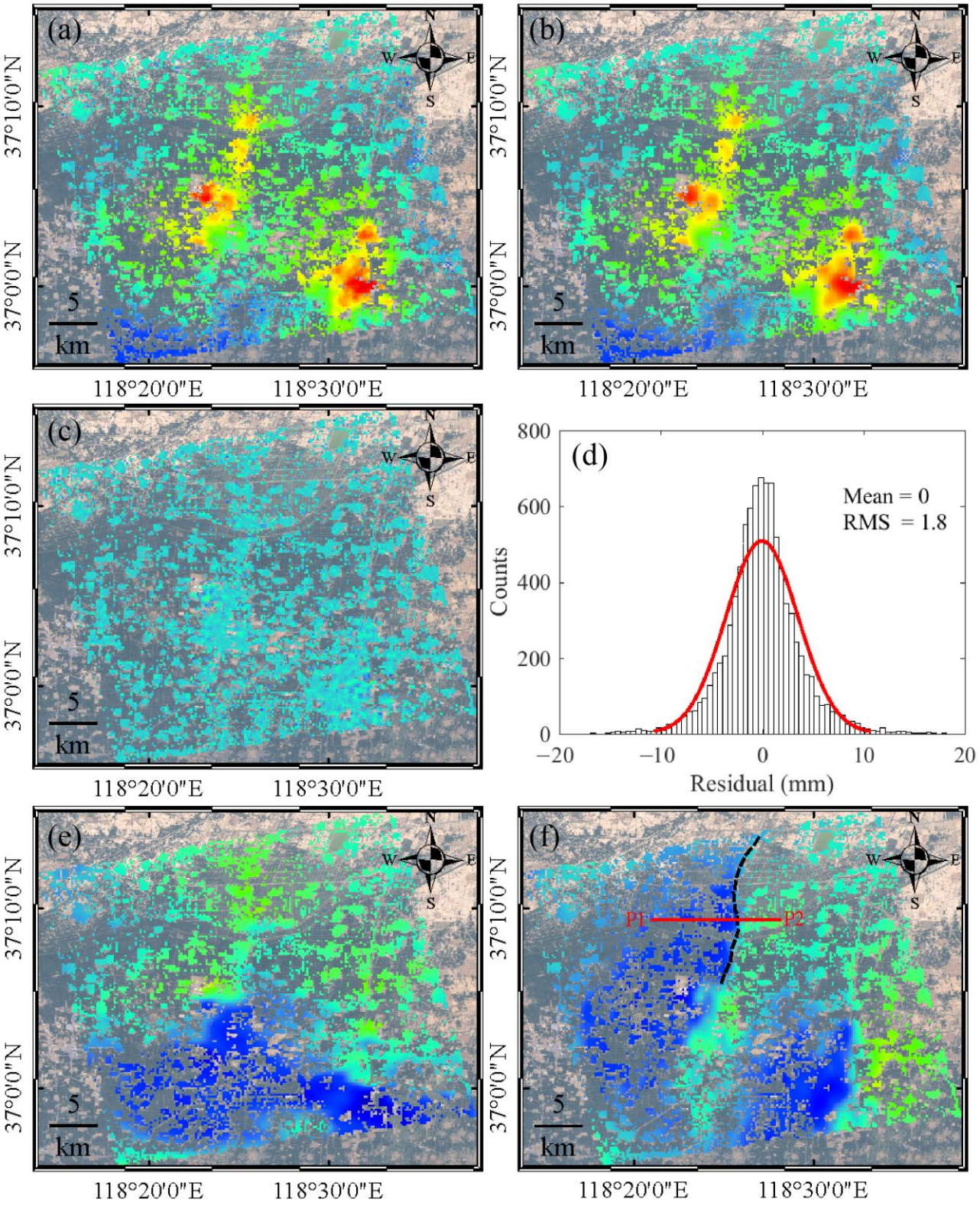

Figure 6. *Cont.*

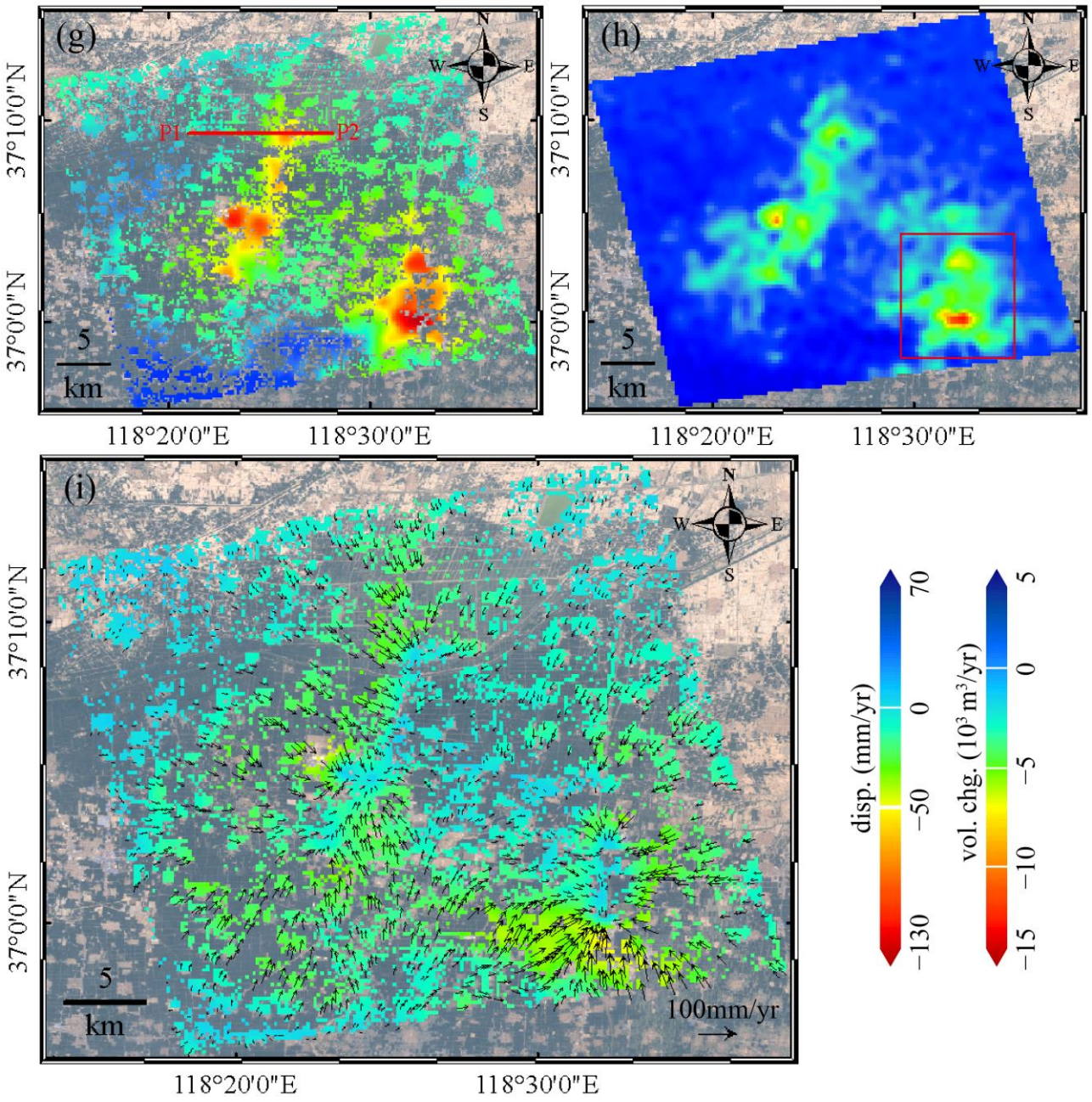

Figure 6. Modeling analysis. (**a**) ALOS InSAR observations. (**b**) Numerical modeling outcomes. (**c**) Residual between (**a**) and (**b**). (**d**) The corresponding histogram of (**c**). (**e**–**g**) depict the modeled north–south-direction, east–west-direction and vertical displacement field maps, respectively. The black dashed curve and red profile line (P1–P2), as in Figure 5, are selected for 3D displacement comparison analysis. (**h**) The modeled volume changes in reservoirs with a burial depth of 350 m, corresponding to the right color bar. The red rectangle denotes the region for the key model variables test in Section 4.1. (**i**) The modeled horizontal displacement field map.

The modeled source volume change indicates a local increase in water storage of up to 2.47×10^3 m^3/year in the blue region (Figure 6h). However, the InSAR observations reveal subsidence ranging from −46.3 to −2.5 mm/year in the study area (Figure 6a), which seems to contradict the volume increase. From a semi-analytical modeling perspective, any surface deformation results from the combined contribution of all model sources through their influence functions (Section 2.5). Therefore, surface subsidence can still occur at a

given point due to the superposition of a remote contracting source with a large volume decrease and a nearby inflating source with a small volume increase.

It is noteworthy that the volume change results are obtained by inverting the observed deformation. The distributed point source model can capture the overall characteristics of the aquifer system and provide a comprehensive distribution of the equivalent volume change in the deep confined aquifer (Figure 6h). The contribution of the volume increase to the deformation is relatively small compared to that of other aquifer units with larger volume decreases. Consequently, subsidence dominates the model area. In addition, spatially, the distribution pattern of regions with significant groundwater extraction is in accordance with that of land subsidence funnels, where the more severe the groundwater depletion, the higher the subsidence rate. Therefore, the combination of InSAR measurements and the distributed point source model can fill the gap between GRACE and field investigations for GS variation monitoring.

4. Discussion

4.1. Impacts of Variable Model Parameters

Detailed reservoir volume change can be efficiently recovered using the distributed point source model constrained by InSAR measurements. The values of multiple key parameters, such as the smoothing factor (α) and grid size, are critical to successful modeling. Therefore, a set of suitable variable values should be selected for modeling in the specified study region. Several interesting findings can be obtained from our simulation experiments.

4.1.1. Smoothing Factor (α)

As the model is discretized and grid points act independently of each other, the smoothing factor (α) plays the role of a trade-off variable between the error of modeling outcomes matching the measurements and the roughness of the spatial distribution of volume change. Six smoothing factors (1,000,000, 1000, 100, 10, 1, and 0.1) are tested for the modeling error-roughness curve. A typical trade-off curve between modeling error and roughness from the modeling is shown in Figure 7a. With the decrease in the smoothing factor, the model error decreases sharply to a stable state while the roughness increases sharply. The smoothing factor, $\alpha = 10$, at the knee of the curve, the point of closest approach of this curve to the origin, is preferentially selected for the final simulation. In addition, the model error-resolution curve is calculated using the same six smoothing factors and is shown in Figure 7b. The model resolution value represents the degree of agreement between inverted model parameters and their true values (see details in Appendix C). That is, the larger the model resolution value, the closer to real data to the model. The plotted curve demonstrates that with the decrease in the smoothing factor, both model error and resolution increase. What is different is that the increase rate of the former increases sharply, while that of the latter decreases gradually. The smoothness factor ($\alpha = 10$) is also at the knee point of this curve, further indicating that the factor value is preferred.

Meanwhile, the corresponding surface displacements can be modeled for different smoothing factors. Figure 8 shows the inversed surface deformation of five typical smoothing factors, indicating that the smaller the smoothing factor, the closer to the observations of the modeled displacements are. Meanwhile, when using a larger smoothing factor, the modeled surface displacements are overly smooth. In addition, the simulated reservoir volume changes can also be simultaneously calculated for the same five factors, which are shown in Figure 9. The reservoir volume changes are highly oscillatory for small smoothing factors, whereas for larger factors, the changes are also overly smooth.

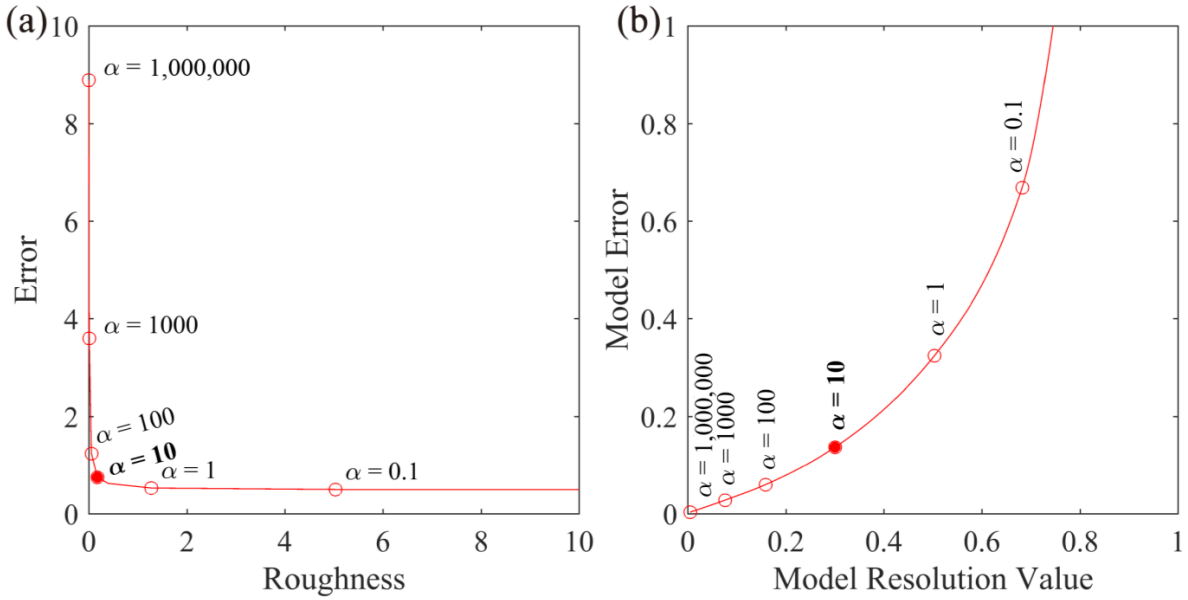

Figure 7. Trade-off curves for modeling to determine the optimal smoothing factor (α). (**a**) Modeling error–roughness curve. The horizontal axis denotes the roughness of the spatial distribution of volume change of the model. The vertical axis denotes the differences between modeling outcomes and InSAR measurements. (**b**) Modeling error-model resolution value curve. The horizontal axis is the model resolution value, which is defined in Appendix C, and represents the degree of agreement between the model and the real data. Both curves are formed by six different Laplacian regularized sources, and each circle represents an individual experiment. The solid red dot represents that a value of 10 is employed as the smoothing factor for the final result.

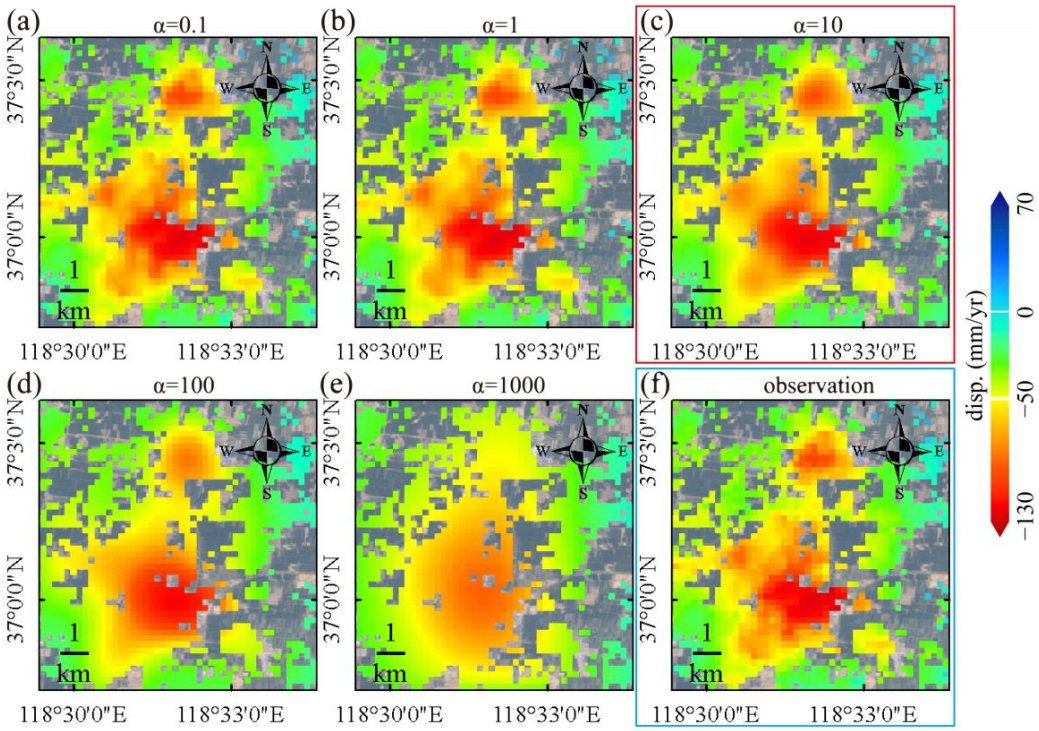

Figure 8. Modeled surface displacement field map using a smoothing factor (α) of (**a**) 0.1, (**b**) 1, (**c**) 10, (**d**) 100, and (**e**) 1000. (**f**) The InSAR measurements. See the red rectangle in Figure 6h for the location. Red and blue rectangle represents the optimal inversion result and InSAR measurements, respectively.

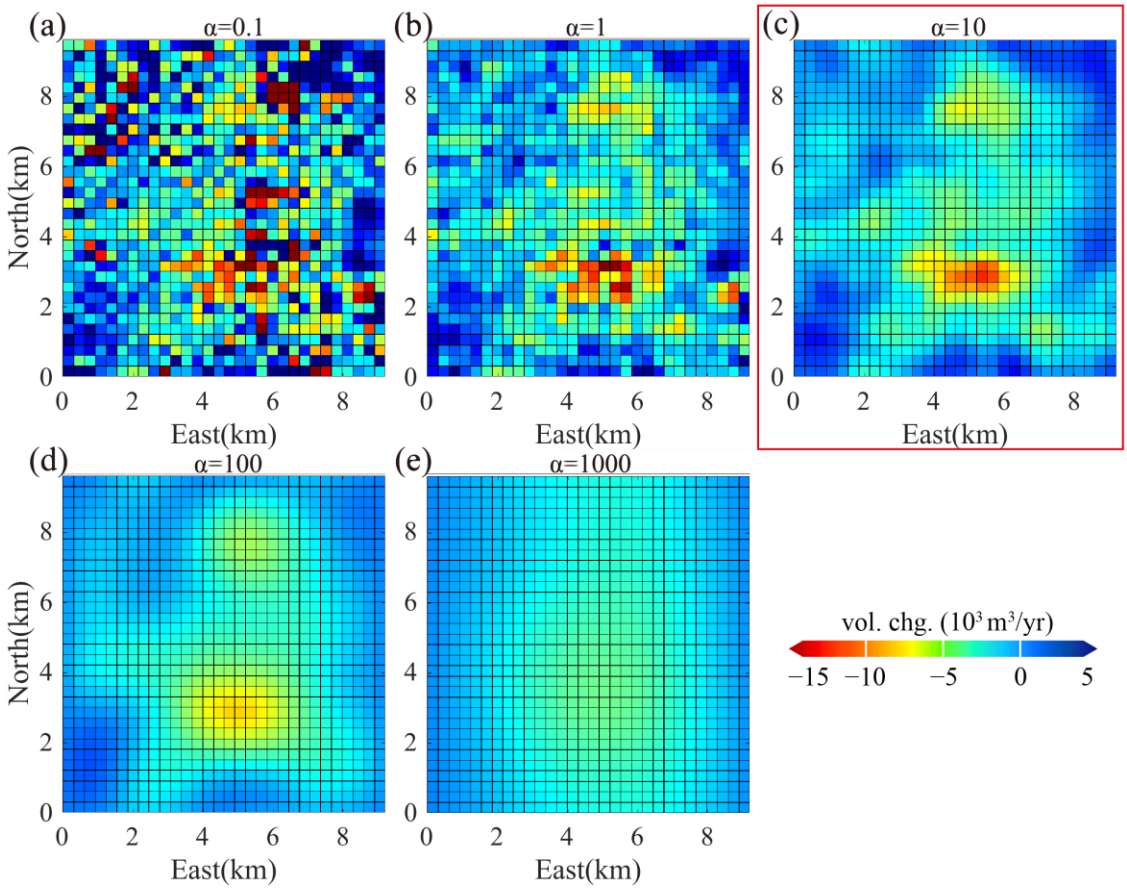

Figure 9. Modeled reservoir volume changes using a smoothing factor (α) of (**a**) 0.1, (**b**) 1, (**c**) 10, (**d**) 100, and (**e**) 1000. The same map extent is used as in Figure 8. Red rectangle represents the optimal inversion result.

Solutions calculated using smoothness factors less than 10 are similar to the observations in Figure 8a,b) but have large model roughness (Figure 7a) and a highly oscillatory volume change (Figure 9a,b). When smoothness factors are larger than 10, both the modeled displacements and reservoir volume changes are overly smoothed (Figures 8d,e and 9d,e), and the former has a large modeling error (Figure 7a), while the latter has small model resolution values (Figure 7b). A smoothing factor of 10, at the knee of the two trade-off curves, yields solutions identical to the InSAR measurements (Figure 8c,f) and a reservoir volume change pattern in accordance with groundwater withdrawal. Therefore, combining these results, a smoothing factor of 10 is the most optimal value and was chosen to obtain the best solution for the reservoir volume change distribution, combining reasonable model resolution and acceptable error.

4.1.2. Reservoir Grid Size

To improve solutions of reservoir volume change modeling for heterogeneous fields using InSAR observations, the reservoir model is discretized into a grid. However, a grid-like pattern is observed in reservoir volume change modeling (Figure 10). So, what is the optimal size of the model mesh? Modeling using reservoir grids with different mesh widths of 400 m, 300 m, 250 m, and 200 m (Figure 10a–d) are examined. It can be seen that, for inverted reservoir volume changes, a grid-like pattern appears and is relatively obvious when the model grid size is large, while serial changes occur for finer grid sizes. However, a fine model grid results in quadratic growth of source numbers, greatly increasing the computational burden in the modeling process. Simultaneously, the trade-off curve of model error vs. model resolution value is calculated and shown in Figure 10e. With the decrease in mesh width, both model error and resolution value decrease. Synthetically,

weighing up these trade-offs carefully, a reservoir grid with a mesh width of 300 m is optimal and is chosen for the final modeling.

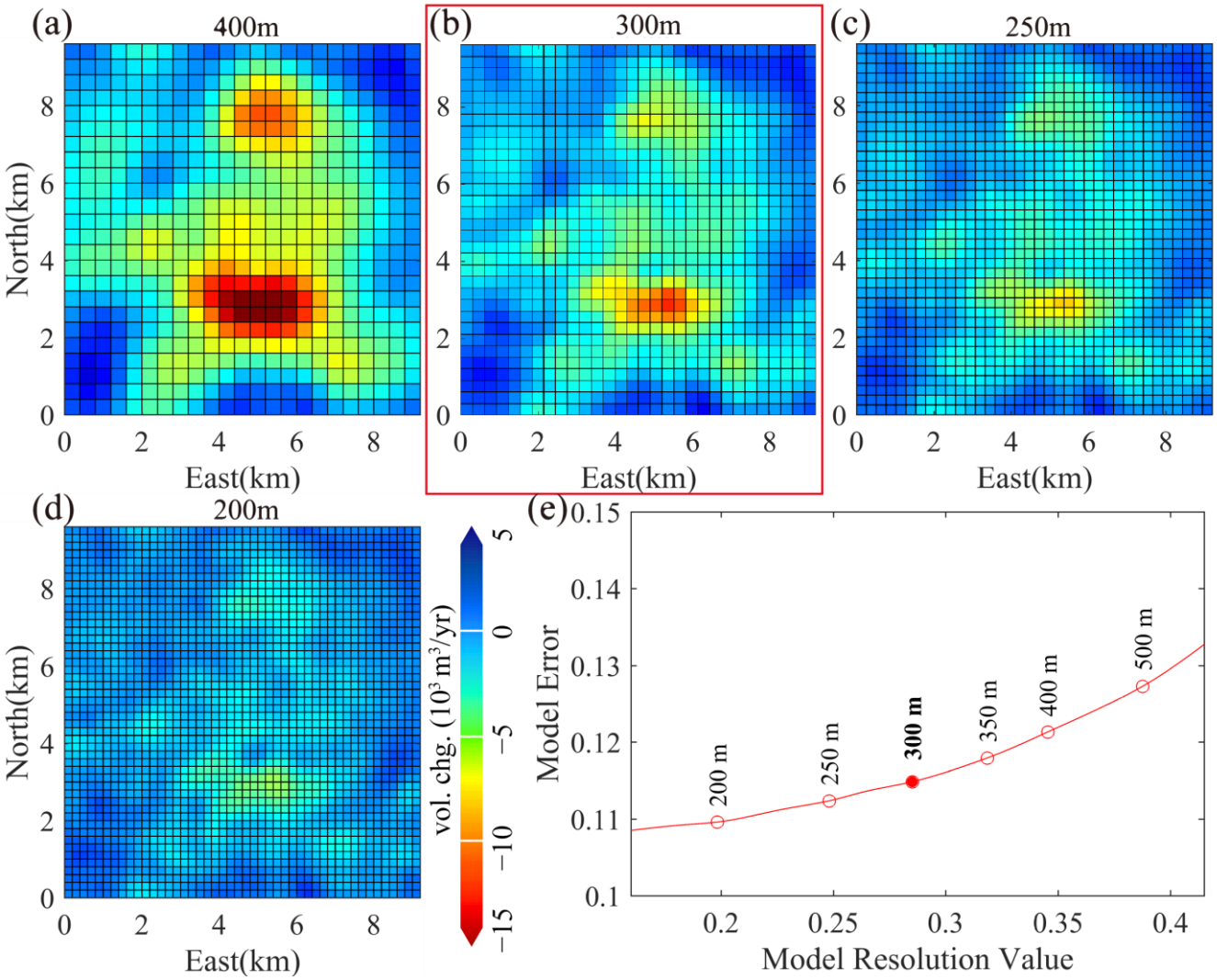

Figure 10. Modeled reservoir volume changes with a mesh width of (**a**) 400 m, (**b**) 300 m, (**c**) 250 m, and (**d**) 200 m. Red rectangle represents the optimal inversion result. (**e**) Trade-off curve between model error and model resolution to determine the model grid size.

4.2. Impacts of Fault and Groundwater

Different values of compressibility of sediment on either side of the fault and low groundwater hydraulic conductivity around the fault cause the fault to be a deformation barrier. Examination of the relationship of the observed land subsidence with the fault can help to address the uneven subsidence, especially the severe regional sinking funnel, that occurred in the study area. Therefore, the displacement field from three different types of images combined with groundwater level and fault data is used for correlation analysis.

InSAR measurements detected multiple remarkable Earth surface sinking regions during the period of 2007 to 2011 in Guangrao (GR), Dongying (DY), Binzhou (BZ), and Boxing (BX), as shown in Figure 11a,b, while remarkable subsidence regions are concentrated largely in the southern part of YRD in the period of 2016 to 2021, such as in GR and BZ (Figure 11c). In particular, persistent settlement occurs in GR, where the spatial distribution pattern and rate of subsidence are similar to each other for both observation periods. Obviously, according to visual inspection, land subsidence has a similar spatial distribution pattern to the faults. GR is controlled by Tonggu Fault (F2) to the north, which

is striking NW and dipping SW, where subsidence velocity changes significantly. DY, a long and narrow abnormal deformation velocity zone, is located in the Central Fault Zone (F4). It consists of several faults striking WE, northern faults dipping S and southern faults dipping N, as shown in Figure 11e, spanning 50–60 km. The northern and southern boundaries of DY coincide with faults to the north and south of the Central Fault Zone, respectively. The southern boundary of BZ and the northern boundary of BX match the northern segment of the Tonggu Fault (F2) and Shicun Fault (F1), respectively. In addition, weak velocity differences occur along the Chennan Fault (F6).

Similarly, the spatial distribution pattern of land subsidence regions is highly consistent with that of the groundwater table funnels (Figure 11a,b,d). That is, typical sinking regions, such as GR, DY, BX, and BZ, are all located in lower-groundwater-level areas. This consistency reveals that groundwater pumping results in a groundwater level decrease and further triggers regional Earth surface subsidence. In addition, groundwater table funnels also have a similar spatial distribution pattern to faults (Figure 11d). Almost all lower groundwater level areas are controlled by Chennan Fault to the north and Paleogene to the south. The groundwater level funnel of Guangrao is bounded by Tonggu Fault to the north. The Dongying groundwater table funnel is located in the Central Fault Zone and is controlled by faults to its north and south. These two typical characteristics in Guangrao and Dongying City are consistent with the features shared between subsidence and faults. Interestingly, the southern part of the Binzhou groundwater funnel is elongated in the SE direction, located in the Chunhua-Caoqiao uplift zone bounded by the Shicun fault to the south and Tonggu fault to the north, implying that the two faults control this aquifer in Binzhou city. All of these findings demonstrate that the subsidence triggered by groundwater withdrawal is controlled by faults in the study area.

Figure 11e depicts the comparative analysis of surface displacement, groundwater level, faults and elevation along the cross-section P3–P4. Significant subsidence regions in the period of 2007 to 2011 are all located in groundwater-level funnels, such as in Guangrao City from 8 to 30 km and Dongying City from 47 to 63 km, while the Earth's surface is relatively stable in higher-groundwater-level areas at 30–47 km and 65–80 km. Moreover, sinking areas and groundwater funnels are both controlled and bounded by faults. The Guangrao subsidence region located in the southern gentle slope zone matches the Tonggu Fault to the north at 30 km during the two periods. In addition, the subsidence curves of the two periods are identical, further showing the continuous Earth surface sinking process caused by groundwater pumping in GR. The Dongying subsidence area during the period of 2007 to 2011 is situated in the Central Fault Zone from 51 to 60 km, where the subsidence curve has a similar shape to the dips of the faults. All of these distinctions further imply that groundwater exploitation can lead to remarkable land subsidence, also affected by faults.

4.3. Impacts of Horizontal Displacement

After the comparative analysis of subsidence with groundwater and faults, a relational analysis between displacement and disasters and the environment can be performed. Both InSAR and modeling results reveal that groundwater pumping can result in significant horizontal displacement, which can further trigger severe damage, such as ground fissures and artificial building cracks. The east–west-direction and vertical displacements can be recovered by both InSAR and modeling, and the cross-section of 2D displacements of InSAR and modeling along the profile line P1–P2 (Figures 5 and 6) in the northern modeling region is shown in Figure 12. The vertical displacements observed by InSAR are identical to those from modeling, and the east-west displacement rate of InSAR is slightly less than that from modeling, further implying that measurable horizontal displacements exist in the study area. The underestimation of InSAR in 5 km is attributed to (i) InSAR monitoring results are more sensitive to vertical deformation and have higher accuracy, while horizontal deformation is relatively less sensitive, (ii) the eliminating of north–south-direction displacement in the computation process of 3D displacements, and (iii) the

heterogeneity of the pressure distribution in the aquifer or spatial variations in the overlying geologic deposits for modeling.

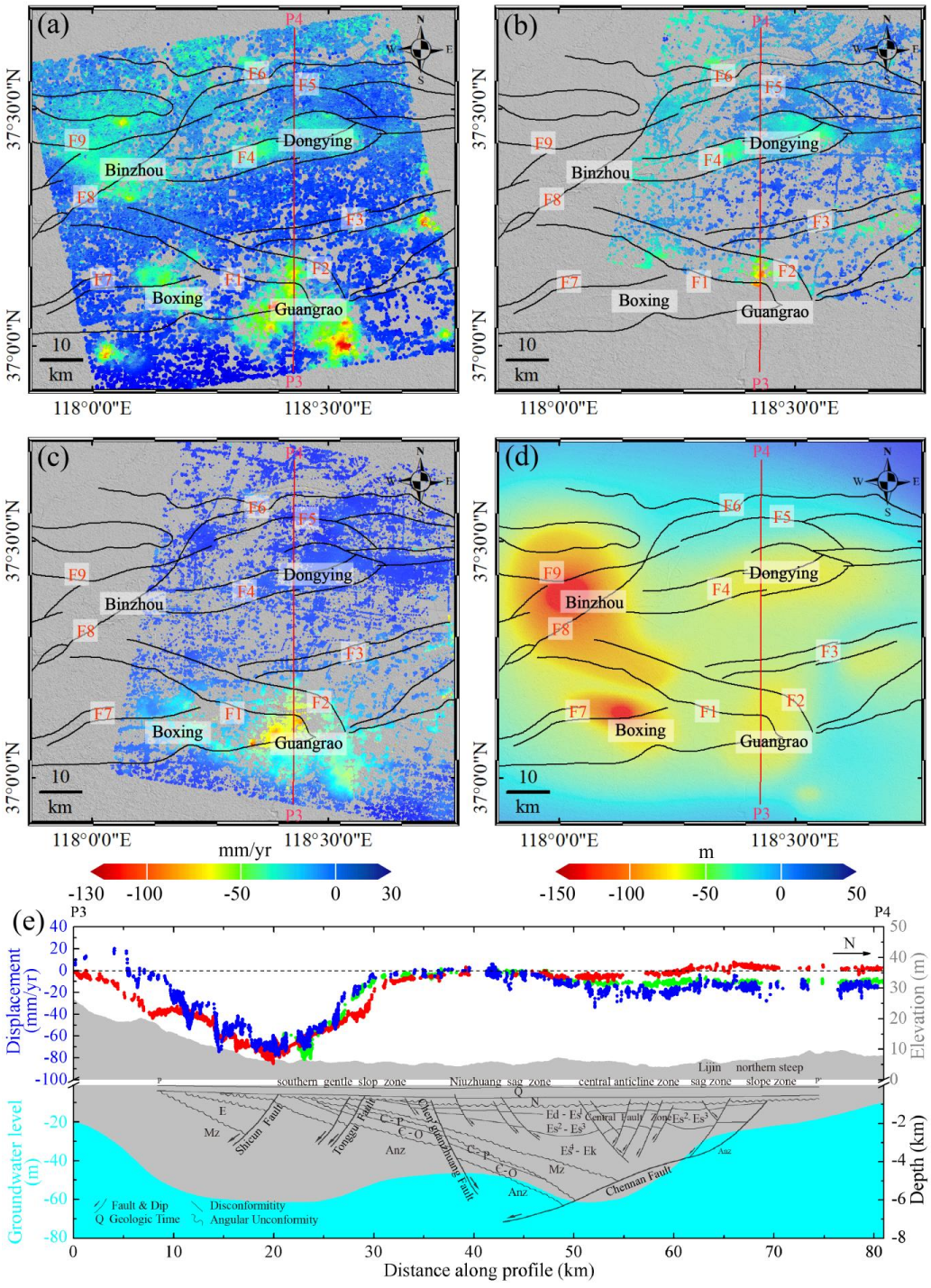

Figure 11. Comparison of Earth surface displacement, faults and groundwater. (**a**–**d**) depict the maps of ALOS observations during the period of 2007 to 2011, ENVISAT measurements for the period of 2007 to 2011, Sentinel-1 outcomes spanning from 2016 to 2011 and the 2009 deep groundwater table, respectively. Faults are overlaid on both figures. For detailed fault information, see Figure 1. (**e**) Cross-section of InSAR measurements (blue, green and red dots, respectively, denote ALOS, ENVISAT and Sentinel-1 results), surface elevation (gray area), the 2009 groundwater table (cyan region) and faults along the line P3–P4. Note the slightly different locations of profile lines P3–P4 in (**a**,**b**) and line P–P′ in Figure 1. For detailed geologic time information, see [65].

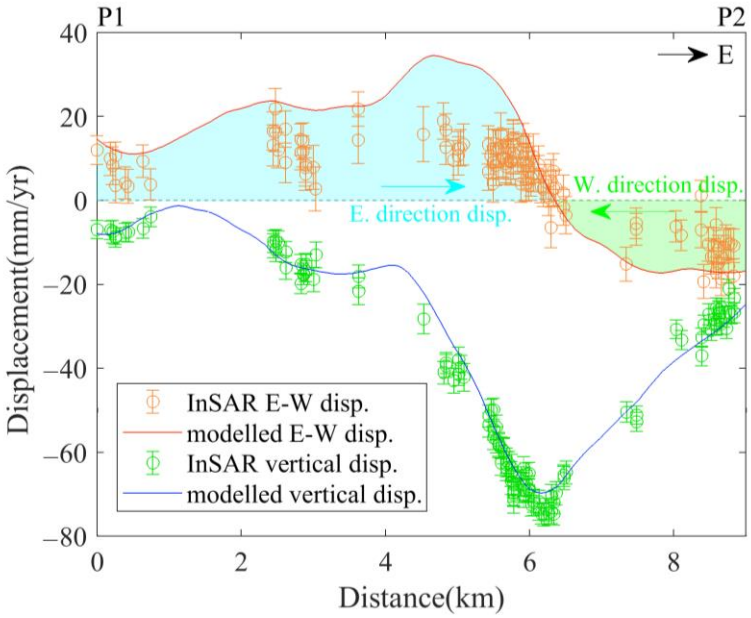

Figure 12. Cross-sectional map of east-west and vertical displacements from InSAR and modeling in line P1–P2. For the location, see Figures 5 and 6.

Spatially, the regional Earth surface deformation is bowl-shaped, whereas the recovered displacement velocity is noncentrosymmetric. The easterly displacement rate (the cyan region in Figure 12) is, in general, larger than the rate of westerly displacement (the green region in Figure 12). Additionally, the western segment of the vertical deformation curve is steeper than the eastern side, revealing that the subsidence velocity gradient in the western region is larger than in the eastern zone. These asymmetric displacements demonstrate that the western part of the bowl-shaped subsidence funnel undergoes relatively larger deformation, which is abundantly clear for the recovered horizontal displacement field (Figure 6i), showing a northeasterly deformation trend. This trend can be explained by the fact that (i) the delta formed progressively seawards, in a northeasterly direction, resulting in "southwest high and northeast low" terrains (e.g., surface elevation of 0–20 km in Figure 11c), (ii) the deposited layer slopes gently in the northeasterly direction, leading to a northeasterly trend of water flow and layer deformation, and (iii) different deposition characteristics of the layers overlying the aquifer. Specifically, the remarkable horizontal displacement has triggered ground fissures [66]. Therefore, Earth surface sinking triggered by groundwater withdrawal, especially horizontal displacement, should be monitored and examined in more detail, further contributing to the more reasonable exploitation and management of groundwater.

5. Conclusions

An integrated analysis of multi-temporal InSAR, distributed point source model, groundwater, and multidisciplinary fault data has been conducted to investigate remarkable land motions and their kinetic regimes in the YRD, and we draw the following conclusions: first, annual InSAR deformation maps during 2007–2021 were derived by ALOS, ENVISAT and Sentinel. More Earth surface information can be detected by multi-temporal InSAR using ALOS images which have a longer wavelength, illustrating multiple significant sinking regions with a maximum displacement velocity of up to 130 mm per year. Second, the spatial distribution pattern and rate of the subsidence in GR and BX during the two periods, 2007–2011 and 2016–2021, are identical, indicating that the significant continuous Earth surface sinking process caused by groundwater extraction exists in the southern part of the YRD. In addition, obvious horizontal displacements can be recovered over GR using a combination of ascending ALOS and descending ENVISAT images, showing an east–west-direction displacement rate of approximately 15 mm per

year. Third, the outcomes from the established numerical model are consistent with InSAR observations, demonstrating that the InSAR-constrained distributed point source model is rational and reliable. A smoothing factor of 10 and a model grid with a mesh width of 300 m are optimal for modeling over the YRD. All of these characteristics are in line with the features of deformation induced by underground reservoir volume or pressure changes. Fourth, the most meaningful outcomes, the annual TWS variations, can be recovered, reaching approximately 12,010 $\times$ 10^3 m^3 in the modeling region. This integrated method can fill the gap between GRACE and field investigations for delta-wide aquifer monitoring. Fifth, faults can act as a barrier to subsidence and aquifers, land subsidence regions, groundwater tables, and faults have a similar spatial distribution pattern in the YRD. The fringes of both land subsidence and the groundwater descent funnel coincide with faults, and the Earth's surface undergoes obvious asymmetric sinking, implying that faults control not only aquifer distribution but also the spatial distribution of regional remarkable land subsidence triggered by groundwater exploitation.

The integrated approach established in this study can primarily allow us to implement a comprehensive combination analysis of advanced InSAR, numerical modeling, and geological, geophysical, and hydrogeological multidisciplinary data in the YRD and further permit us to characterize the Earth surface displacement pattern, providing insights into its dynamic laws and mechanisms, as well as the role of faults and groundwater consumption in the action of surface sinking and aquifer changes. In particular, this multidisciplinary approach is economic, precise and efficient in monitoring Earth's surface deformation and aquifer changes, playing a significant part in disaster risk assessment, warning and control, and sustainable groundwater management.

Author Contributions: Conceptualization, Y.L. and R.D.; methodology, Y.L. and Y.N.; software, Y.L., Y.N. and F.Q.; validation, Y.Z. and F.Z.; formal analysis, Y.L., R.D. and L.Z.; investigation, Y.L. and Y.N.; resources, R.D. and Z.L.; data curation, R.D. and Z.L.; writing—original draft preparation, Y.L.; writing—review and editing, Y.L., R.D. and Z.L.; visualization, R.D.; supervision, L.Z.; project administration, L.Z.; funding acquisition, Y.L., R.D. and L.Z. All authors have read and agreed to the published version of the manuscript.

Funding: This research was funded by Open Fund of the Key Laboratory of Marine Geology and Environment, Chinese Academy of Sciences (No. MGE2022KG1), Major Research Plan on West-Pacific Earth System Multispheric Interactions, grant number 92058213, National Natural Science Foundation of China, grant numbers 41706092, 41676039, 41930535, and 42006148, and Shandong Provincial Natural Science Foundation, grant number ZR2022QD087.

Data Availability Statement: The sentinel 1 data in this study were obtained by ESA Copernicus data hub. Satellite precise orbit data is available at https://qc.sentinel1.eo.esa.int/aux_poeorb. SRTM1 data can be downloaded at https://earthexplorer.usgs.gov/ (all accessed on 29 December 2021).

Acknowledgments: ENVISAT SAR data were acquired under the Category 1 research project C1F.19709 from the European Space Agency. ALOS/PALSAR data are copyrighted by JAXA and were provided by Alaska Satellite Facility. Sentinel data were provided by European Space Agency. We thank JPL for ROI_PAC, DEOS for DORIS, Andy Hooper for StaMPS, and the National Geological Archives of China and Shandong Provincial Lubei Geo-engineering Exploration Institute for providing relevant geological, hydrological, and leveling data. The constructive comments of the two anonymous reviewers are also gratefully acknowledged for significantly helping to improve the original paper.

Conflicts of Interest: The authors declare no conflict of interest.

Appendix A

Table A1. Partition of geological engineering stratums.

Stratigraphic Age	Burial Depth of Floor (m)	Thickness (m)	Lithology
Holocene			
Q43	1.1–2.0	1.1–2.0	Silty clay, silt
	2.0–4.0	1.0–2.0	
Q42	7.0–9.0	4.0–6.0	Silt, silty clay
	14.0–16.0	6.0–8.0	
	18.4–28.8	4.0–8.0	
Q41	25.2–31.8	2.0–10.3	Fine sand
Late pleistocene			
Q32	36.0–41.0	8.0–11.0	Silty clay, silt
	45.0–50.0	8.0–10.0	
	60.0–70.8	10.0–13.0	
Q31	85.0–90.0	23.0–28.0	Silty-fine sand, silty clay
	110–118	25.0–30.0	
Middle pleistocene			
Q2	150–160	38.0–45.0	Silty clay, sand layer
Early pleistocene			
Q1	300–330	145–170	
Pliocene			
Nm3	400–460	105–150	
Nm2	600–650	180–220	Mid-fine sand, clay
Nm1	900–1000	280–380	Clay, mid-fine sand

Appendix B

Validation of InSAR results against on-field leveling survey measurements along two leveling lines (Figure A1) is conducted to assess the accuracy and reliability of the InSAR measurements. InSAR results compare well with leveling data (Figure A2), suggesting the multi-temporal InSAR observations are reliable and precise.

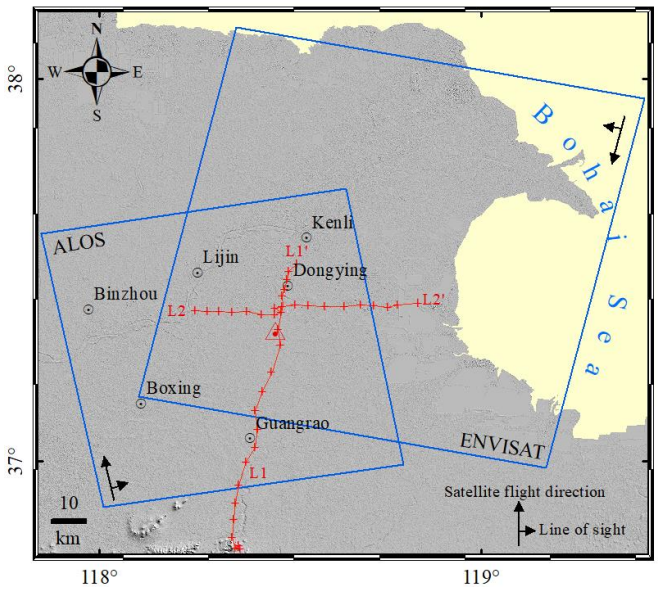

Figure A1. Sketch map of leveling lines for validation of InSAR observations. Blue rectangle and red line represents the InSAR coverage and leveling line, respectively.

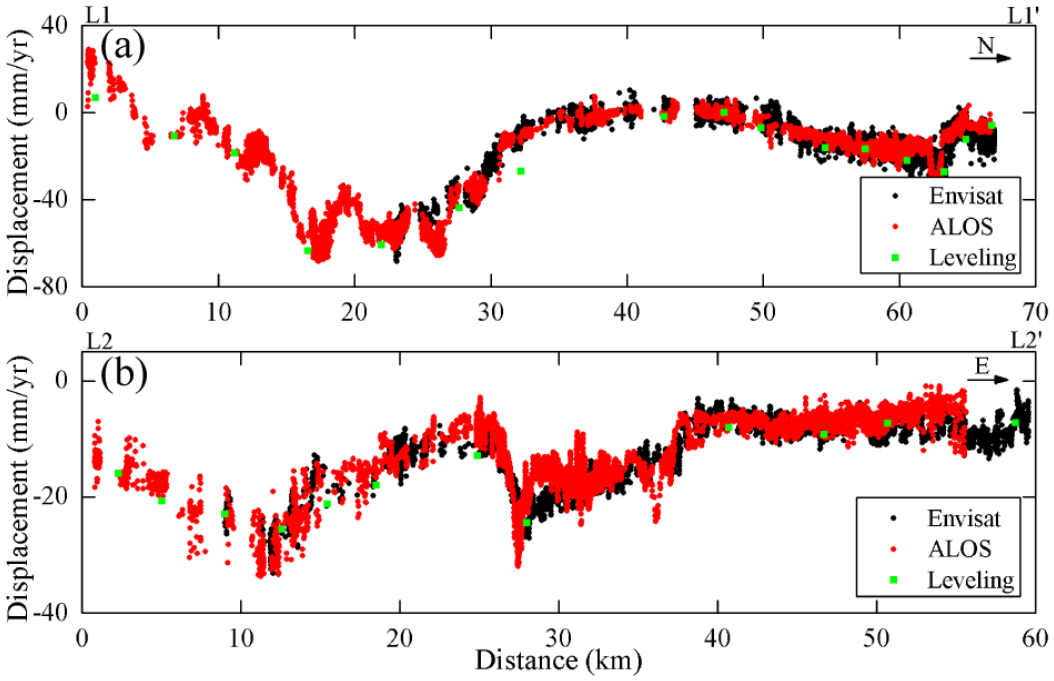

Figure A2. InSAR results validation with leveling data. (**a**) Elevation change along a south-to-north path (L1–L1′ in Figure A1). (**b**) Elevation change along a west-to-east path (L2–L2′ in Figure A1).

Appendix C

The model resolution matrix (M) correlates the estimated values (S^{model}) to their real values (S^{real}), is defined as $S^{model} = M \cdot S^{real}$, and calculated by $M = ((G^{los})^T G^{los} + \alpha L^T L)^{-1} (G^{los})^T G^{los}$. The model resolution, which was calculated during the inversion process, is 0.29.

References

1. Giosan, L.; Syvitski, J.; Constantinescu, S.; Day, J. Climate change: Protect the world's deltas. *Nature* **2014**, *516*, 31–33. [CrossRef]
2. Syvitski, J.P.M. Deltas at risk. *Sustain. Sci.* **2008**, *3*, 23–32. [CrossRef]
3. Minderhoud, P.S.J.; Middelkoop, H.; Erkens, G.; Stouthamer, E. Groundwater extraction may drown mega-delta: Projections of extraction-induced subsidence and elevation of the Mekong delta for the 21st century. *Environ. Res. Commun.* **2020**, *2*, 011005. [CrossRef]
4. Erban, L.E.; Gorelick, S.M.; Zebker, H.A.; Fendorf, S. Release of arsenic to deep groundwater in the Mekong Delta, Vietnam, linked to pumping-induced land subsidence. *Proc. Natl. Acad. Sci. USA* **2013**, *110*, 13751–13756. [CrossRef] [PubMed]
5. Syvitski, J.P.M.; Kettner, A.J.; Overeem, I.; Hutton, E.W.H.; Hannon, M.T.; Brakenridge, G.R.; Day, J.; Vorosmarty, C.; Saito, Y.; Giosan, L.; et al. Sinking deltas due to human activities. *Nat. Geosci.* **2009**, *2*, 681–686. [CrossRef]
6. IPCC. *Climate Change 2014: Synthesis Report. Contribution of Working Groups I, II and III to the Fifth Assessment Report of the Intergovernmental Panel on Climate Change*; Pachauri, R.K., Meyer, L.A., Core Writing Team, Eds.; IPCC: Geneva, Switzerland, 2014; p. 151.
7. Wong, P.P.; Losada, I.J.; Gattuso, J.-P.; Hinkel, J.; Khattabi, A.; McInnes, K.L.; Saito, Y.; Sallenger, A. *Coastal systems and low-lying areas, in Climate Change 2014: Impacts, Adaptation, and Vulnerability. Part A: Global and Sectoral Aspects. Contribution of Working Group II to the Fifth Assessment Report of the Intergovernmental Panel on Climate Change*; Field, C.B., Barros, V.R., Dokken, D.J., Mach, K.J., Mastrandrea, M.D., Bilir, T.E., Chatterjee, M., Ebi, K.L., Estrada, Y.O., Genova, R.C., et al., Eds.; Cambridge University Press: Cambridge, UK; New York, NY, USA, 2014; pp. 361–409.
8. UNESCO/UN-Water. *United Nations World Water Development Report 2020: Water and Climate Change*; UNESCO: Paris, France, 2020.
9. Zhang, Y.; Liu, Y.; Zhang, X.; Huang, H.; Qin, K.; Bai, Z.; Zhou, X. Correlation Analysis between Land-Use/Cover Change and Coastal Subsidence in the Yellow River Delta, China: Reviewing the Past and Prospecting the Future. *Remote Sens.* **2021**, *13*, 4563. [CrossRef]

10. Lazos, I.; Papanikolaou, I.; Sboras, S.; Foumelis, M.; Pikridas, C. Geodetic Upper Crust Deformation Based on Primary GNSS and INSAR Data in the Strymon Basin, Northern Greece—Correlation with Active Faults. *Appl. Sci.* **2022**, *12*, 9391. [CrossRef]
11. Shen, G.; Fu, W.; Guo, H.; Liao, J. Water Body Mapping Using Long Time Series Sentinel-1 SAR Data in Poyang Lake. *Water* **2022**, *14*, 1902. [CrossRef]
12. Dixon, T.H.; Amelung, F.; Ferretti, A.; Novali, F.; Rocca, F.; Dokka, R.; Sella, G.; Kim, S.-W.; Wdowinski, S.; Whitman, D. Subsidence and flooding in New Orleans. *Nature* **2006**, *441*, 587–588. [CrossRef]
13. Teatini, P.; Tosi, L.; Strozzi, T. Quantitative evidence that compaction of Holocene sediments drives the present land subsidence of the Po Delta, Italy. *J. Geophys. Res. Solid Earth* **2011**, *116*, B08407. [CrossRef]
14. Higgins, S.A. Review: Advances in delta-subsidence research using satellite methods. *Hydrogeol. J.* **2016**, *24*, 587–600. [CrossRef]
15. Qu, F.; Lu, Z.; Kim, J.; Turco, M.J. Mapping and characterizing land deformation during 2007–2011 over the Gulf Coast by L-band InSAR. *Remote Sens. Environ.* **2023**, *284*, 113342. [CrossRef]
16. Qu, F.F.; Lu, Z.; Zhang, Q.; Bawden, G.W.; Kim, J.-W.; Zhao, C.Y.; Qu, W. Mapping ground deformation over Houston–Galveston, Texas using multi-temporal InSAR. *Remote Sens. Environ.* **2015**, *169*, 290–306. [CrossRef]
17. Massonnet, D.; Feigl, K.L. Radar interferometry and its application to changes in the Earth's surface. *Rev. Geophys.* **1998**, *36*, 441–500. [CrossRef]
18. Hooper, A.; Bekaert, D.; Spaans, K.; Arıkan, M. Recent advances in SAR interferometry time series analysis for measuring crustal deformation. *Tectonophysics* **2012**, *514–517*, 1–13. [CrossRef]
19. Gebremichael, E.; Sultan, M.; Becker, R.; El Bastawesy, M.; Cherif, O.; Emil, M. Assessing Land Deformation and Sea Encroachment in the Nile Delta: A Radar Interferometric and Inundation Modeling Approach. *J. Geophys. Res. Solid Earth* **2018**, *123*, 3208–3224. [CrossRef]
20. Liu, Y.L.; Huang, H.J.; Liu, Y.X.; Bi, H.B. Linking land subsidence over the Yellow River delta, China, to hydrocarbon exploitation using multi-temporal InSAR. *Nat. Hazards* **2016**, *84*, 271–291. [CrossRef]
21. Fabris, M.; Battaglia, M.; Chen, X.; Menin, A.; Monego, M.; Floris, M. An Integrated InSAR and GNSS Approach to Monitor Land Subsidence in the Po River Delta (Italy). *Remote Sens.* **2022**, *14*, 5578. [CrossRef]
22. Ferretti, A.; Monti-Guarnieri, A.; Prati, C.; Rocca, F.; Massonet, D. *InSAR Principles-Guidelines for SAR Interferometry Processing and Interpretation*; Fletcher, K., Ed.; ESA Publications: Noordwijk, The Netherlands, 2007; Volume 19.
23. Ferretti, A.; Prati, C.; Rocca, F. Permanent scatterers in SAR interferometry. *Geosci. Remote Sens. IEEE Trans.* **2001**, *39*, 8–20. [CrossRef]
24. Berardino, P.; Fornaro, G.; Lanari, R.; Sansosti, E. A new algorithm for surface deformation monitoring based on small baseline differential SAR interferograms. *Geosci. Remote Sens. IEEE Trans.* **2002**, *40*, 2375–2383. [CrossRef]
25. Hooper, A. A multi-temporal InSAR method incorporating both persistent scatterer and small baseline approaches. *Geophys. Res. Lett.* **2008**, *35*, L16302. [CrossRef]
26. Hooper, A.; Zebker, H.; Segall, P.; Kampes, B. A new method for measuring deformation on volcanoes and other natural terrains using InSAR persistent scatterers. *Geophys. Res. Lett.* **2004**, *31*, L23611. [CrossRef]
27. Hooper, A.; Segall, P.; Zebker, H. Persistent scatterer interferometric synthetic aperture radar for crustal deformation analysis, with application to Volcán Alcedo, Galápagos. *J. Geophys. Res. Solid Earth (1978–2012)* **2007**, *112*, B07407. [CrossRef]
28. IPCC. *Climate Change 2007: Impacts, Adaptation and Vulnerability. Contribution of Working Group II to the Fourth Assessment Report of the Intergovernmental Panel on Climate Change*; Canziani, O.F., Parry, M.L., Palutikof, J.P., van der Linden, P.J., Hanson, C.E., Richard, J., Eds.; Cambridge University Press: Cambridge, UK, 2007; p. 976.
29. Liu, Y.L.; Huang, H.J.; Dong, J.F. Large-area land subsidence monitoring and mechanism research using the small baseline subset interferometric synthetic aperture radar technique over the Yellow River Delta, China. *J. Appl. Remote Sens.* **2015**, *9*, 096019. [CrossRef]
30. Scanlon, B.R.; Faunt, C.C.; Longuevergne, L.; Reedy, R.C.; Alley, W.M.; McGuire, V.L.; McMahon, P.B. Groundwater depletion and sustainability of irrigation in the US High Plains and Central Valley. *Proc. Natl. Acad. Sci. USA* **2012**, *109*, 9320–9325. [CrossRef] [PubMed]
31. Tapley, B.D.; Bettadpur, S.; Ries, J.C.; Thompson, P.F.; Watkins, M.M. GRACE Measurements of Mass Variability in the Earth System. *Science* **2004**, *305*, 503–505. [CrossRef]
32. Tapley, B.D.; Watkins, M.M.; Flechtner, F.; Reigber, C.; Bettadpur, S.; Rodell, M.; Sasgen, I.; Famiglietti, J.S.; Landerer, F.W.; Chambers, D.P.; et al. Contributions of GRACE to understanding climate change. *Nat. Clim. Chang.* **2019**, *9*, 358–369. [CrossRef]
33. Scanlon, B.R.; Zhang, Z.; Save, H.; Sun, A.Y.; Müller Schmied, H.; van Beek, L.P.H.; Wiese, D.N.; Wada, Y.; Long, D.; Reedy, R.C.; et al. Global models underestimate large decadal declining and rising water storage trends relative to GRACE satellite data. *Proc. Natl. Acad. Sci. USA* **2018**, *115*, E1080–E1089. [CrossRef]
34. Rodell, M.; Velicogna, I.; Famiglietti, J.S. Satellite-based estimates of groundwater depletion in India. *Nature* **2009**, *460*, 999–1002. [CrossRef]
35. Poland, J.F.; Davis, G.H. Land subsidence due to withdrawal of fluids. *Rev. Eng. Geol.* **1969**, *2*, 187–270. [CrossRef]
36. Galloway, D.; Burbey, T. Review: Regional land subsidence accompanying groundwater extraction. *Hydrogeol. J.* **2011**, *19*, 1459–1486. [CrossRef]

37. Bawden, G.W.; Thatcher, W.; Stein, R.S.; Hudnut, K.W.; Peltzer, G. Tectonic contraction across Los Angeles after removal of groundwater pumping effects. *Nature* **2001**, *412*, 812–815. [CrossRef] [PubMed]
38. Motagh, M.; Shamshiri, R.; Haghshenas Haghighi, M.; Wetzel, H.-U.; Akbari, B.; Nahavandchi, H.; Roessner, S.; Arabi, S. Quantifying groundwater exploitation induced subsidence in the Rafsanjan plain, southeastern Iran, using InSAR time-series and in situ measurements. *Eng. Geol.* **2017**, *218*, 134–151. [CrossRef]
39. Qu, F.F.; Zhang, Q.; Lu, Z.; Zhao, C.Y.; Yang, C.S.; Zhang, J. Land subsidence and ground fissures in Xi'an, China 2005–2012 revealed by multi-band InSAR time-series analysis. *Remote Sens. Environ.* **2014**, *155*, 366–376. [CrossRef]
40. De Wit, K.; Lexmond, B.R.; Stouthamer, E.; Neussner, O.; Dörr, N.; Schenk, A.; Minderhoud, P.S.J. Identifying Causes of Urban Differential Subsidence in the Vietnamese Mekong Delta by Combining InSAR and Field Observations. *Remote Sens.* **2021**, *13*, 189. [CrossRef]
41. Minderhoud, P.S.J.; Hlavacova, I.; Kolomaznik, J.; Neussner, O. Towards unraveling total subsidence of a mega-delta—The potential of new PS InSAR data for the Mekong delta. *Proc. Int. Assoc. Hydrol. Sci.* **2020**, *382*, 327–332. [CrossRef]
42. Liu, Y.; Liu, J.; Xia, X.; Bi, H.; Huang, H.; Ding, R.; Zhao, L. Land subsidence of the Yellow River Delta in China driven by river sediment compaction. *Sci. Total Environ.* **2021**, *750*, 142165. [CrossRef]
43. Milliman, J.D.; Syvitski, J.P.M. Geomorphic/Tectonic Control of Sediment Discharge to the Ocean: The Importance of Small Mountainous Rivers. *J. Geol.* **1992**, *100*, 525–544. [CrossRef]
44. Ganti, V.; Chu, Z.; Lamb, M.P.; Nittrouer, J.A.; Parker, G. Testing morphodynamic controls on the location and frequency of river avulsions on fans versus deltas: Huanghe (Yellow River), China. *Geophys. Res. Lett.* **2014**, *41*, 7882–7890. [CrossRef]
45. Fan, H.; Huang, H.J.; Zeng, T.Q.; Wang, K.R. River mouth bar formation, riverbed aggradation and channel migration in the modern Huanghe (Yellow) River delta, China. *Geomorphology* **2006**, *74*, 124–136. [CrossRef]
46. Zhang, H.; Liu, X.; Jia, Y.; Du, Q.; Sun, Y.; Yin, P.; Shan, H. Rapid consolidation characteristics of Yellow River-derived sediment: Geotechnical characterization and its implications for the deltaic geomorphic evolution. *Eng. Geol.* **2020**, *270*, 105578. [CrossRef]
47. Zhang, S.W. The application of an integrated approach in exploration of lacustrine turbidites in Jiyang Sub-basin, Bohai Bay Basin, China. *J. Pet. Sci. Eng.* **2004**, *41*, 67–77. [CrossRef]
48. Zhang, L.Y.; Liu, Q.; Zhu, R.F.; Li, Z.; Lu, X.C. Source rocks in Mesozoic–Cenozoic continental rift basins, east China: A case from Dongying Depression, Bohai Bay Basin. *Org. Geochem.* **2009**, *40*, 229–242. [CrossRef]
49. Li, S.N.; Wang, G.X.; Deng, W.; Lu, Y.X. Variations of Groundwater Depth in Yellow River Delta in Recent Two Decades. *Prog. Geogr.* **2008**, *27*, 49–56, (In Chinese with English Abstract).
50. DBDMPG. Dongying Book, Dongying Municipal People's Government. 2021. Available online: http://www.dongying.gov.cn/dynj/dynj2006-g1/index.html#p=50 (accessed on 20 May 2020). (In Chinese)
51. DODMPG. Dongying Overview, Dongying Municipal People's Government. 2021. Available online: http://www.dongying.gov.cn/col/col40583/index.html (accessed on 23 April 2021). (In Chinese)
52. Hooper, A.; Zebker, H.A. Phase unwrapping in three dimensions with application to InSAR time series. *J. Opt. Soc. Am. A* **2007**, *24*, 2737–2747. [CrossRef]
53. Fuhrmann, T.; Garthwaite, M.C. Resolving Three-Dimensional Surface Motion with InSAR: Constraints from Multi-Geometry Data Fusion. *Remote Sens.* **2019**, *11*, 241. [CrossRef]
54. Mogi, K. Relations between the eruptions of various volcanoes and the deformations of the ground surfaces around them. *Bull. Earthq. Res. Inst. Univ. Tokyo* **1958**, *36*, 99–134.
55. Terzaghi, K.; Ralph, B.P.; Gholamreza, M. *Soil Mechanics in Engineering Practice*; JohnWiley & Sons: Hoboken, NJ, USA, 1996.
56. Segall, P. *Earthquake and Volcano Deformation*; Princeton University Press: Princeton, NJ, USA, 2010.
57. Fokker, P.A.; Orlic, B. Semi-Analytic Modelling of Subsidence. *Math. Geol.* **2006**, *38*, 565–589. [CrossRef]
58. Du, Y.; Aydin, A.; Segall, P. Comparison of various inversion techniques as applied to the determination of a geophysical deformation model for the 1983 Borah Peak earthquake. *Bull. Seismol. Soc. Am.* **1992**, *82*, 1840–1866. [CrossRef]
59. Geertsma, J. Land subsidence above compacting oil and gas reservoirs. *J. Pet. Technol.* **1973**, *25*, 734–744. [CrossRef]
60. Dusseault, M.; Rothenburg, L. Analysis of Deformation Measurements for Reservoir Managemen. *Oil Gas Sci. Technol.* **2002**, *57*, 539–554. [CrossRef]
61. Zhang, Y.; Huang, H.; Liu, Y.; Liu, Y.; Bi, H. Spatial and temporal variations in subsidence due to the natural consolidation and compaction of sediment in the yellow river delta, china. *Mar. Georesour. Geotechnol.* **2018**, *37*, 152–163. [CrossRef]
62. Liu, Y.; Du, T.; Huang, H.; Liu, Y.; Zhang, Y. Estimation of sediment compaction and its relationship with river channel distributions in the Yellow River delta, China. *Catena* **2019**, *182*, 104113. [CrossRef]
63. Dijkstra, T.K. Latent Variables and Indices: Herman Wold's Basic Design and Partial Least Squares. In *Handbook of Partial Least Squares*; Esposito, V.V., Chin, W., Henseler, J., Wang, H., Eds.; Springer Handbooks of Computational Statistics; Springer: Berlin/Heidelberg, Germany, 2010; pp. 23–46. [CrossRef]
64. SPGEMS. *Report on the Investigation and Evaluation of Environmental Geological Issues in Key Groundwater Extraction Areas in Shandong Province*; Shandong Provincial Geological Environment Monitoring Station: Jinan, China, 2013. (In Chinese)

65. Zhang, S.W.; Wang, Y.S.; Shi, D.S.; Xu, H.M.; Pang, X.Q.; Li, M.W. Fault-fracture mesh petroleum plays in the Jiyang Superdepression of the Bohai Bay Basin, eastern China. *Mar. Pet. Geol.* **2004**, *21*, 651–668. [CrossRef]
66. An, H.; Wang, B.; Changlong, Z. Study on Forming Mechanism of Structural Type Ground Fissures in Shandong Province. *Shandong Land Resour.* **2014**, *32*, 34–37, (In Chinese with English Abstract).